

A Triboelectric-based Method for Rapid Characterization of Powders

A Triboelectric-based Method for Rapid Characterization of Powders

By
Hadi Mehrtash, B. ENG

A Thesis
Submitted to the School of Graduate Studies
in Partial Fulfillment of the Requirements
for the Degree of
Master of Applied Science
in Mechanical Engineering

McMaster University
© Copyright by Hadi Mehrtash,
August 2021

Master of Applied Science (2021)
(Mechanical Engineering)

McMaster University
Hamilton, Ontario

TITLE: A Triboelectric-based Method for
Rapid Characterization of
Powders

AUTHOR: Hadi Mehrtash

B. Eng (McMaster University)

SUPERVISORS: Dr. Amin Rajabzadeh

Dr. Seshasai Srinivasan

NUMBER OF PAGES: i- 105

Abstract

The triboelectrification of powders, which is typically caused by interparticle collisions and particle-wall interactions is often known as a nuisance phenomenon, especially during the powder handling process in different industries. Particularly in the pharmaceutical industry, wall-fouling occurs due to the electrostatic charging of particles during transport in particle-laden pipe flows, leading to inconsistencies in final product dosage. Dust explosions due to excessive powder charging also pose a severe hazard causing damages to personnel, infrastructure, and equipment. In the polyolefin industry, sheet formation on the reactor walls due to particle charging combined with extremely exothermic polymerization reactions negatively affect the reactor's performance resulting in reactor shutdown. Electrostatic charge generation in particle-laden pipe flows has been broadly studied throughout the years; however, little attention has been paid to utilizing this natural phenomenon as a tool for the characterization of powders' physical and chemical properties, which is the focus of this study. Modeling particle tribocharging based on the chemical and physical properties of particles and the hydrodynamic of the system would considerably help provide insight into the influence of different parameters on the charging behavior of powders. Integrating a computational fluid dynamics (CFD) model for simulating particles motion in a carrier fluid with a tribocharging model can be used not only as a predictive tool in the industry but as a rapid and cost-effective method for powder characterization.

In this research, a tribocharging model based on the prominent condenser model was used in combination with an Eulerian-Lagrangian CFD model to simulate particle tribocharging in particle-laden flows. The influence of different parameters on particle-wall interactions during particle transport in a particle-laden pipe flow was elucidated. An artificial neural network was developed for predicting particle-wall collision numbers based on a database obtained through CFD simulations. The particle-wall collision number from the CFD model was validated against experimental data in the literature. The tribocharging and CFD models were coupled with the experimental tribocharging data to estimate the contact potential difference of powders, which is a function of contact surfaces' work functions and depends on the physicochemical properties of materials. While the contact potential difference between the particles and wall

is an essential parameter in the tribocharging models, the accurate measurement of the property is a complex process requiring a highly controlled environment and special equipment. The results from this research also confirm that particle tribocharging is very much dependant on the particle-wall collision number influenced by various parameters, such as particle size and density, air velocity, and pipe dimensions. Plotting the experimentally measured charge-to-mass ratios against the calculated contact potential differences for samples with different protein contents uncovered a linear trend, which opens a novel approach for protein quantification of powders for a given particle size. Therefore, an algorithm is proposed for rapid quantification of protein content and particle size determination of samples during transport in particle-laden flows based on the triboelectric charge measurement. The algorithm requires a CFD-based artificial neural network to estimate the particle-wall interactions based on the hydrodynamic characteristics of the particles and flow systems.

Acknowledgment

First and foremost, I would like to thank my supervisors, Dr. Amin Rajabzadeh and Dr. Seshasai Srinivasan. I was fortunate to have them as supervisors who dedicated so much of their time to help me. Without their support and constant help this dissertation would not have been possible. They encouraged me to grow as an independent thinker and provided me with the foundation to become a researcher. I would like to thank the Department of Mechanical Engineering at McMaster University.

Lastly, I wish to thank my family, who helped shape me into the person I am today. My mother, Farkhondeh, and my father, Sadegh, for their unconditional love and support throughout my life. My brothers, Moein and Mostafa, for inspiring me to tackle any and all obstacles set before me. Finally, I wish to thank my amazing wife, Farzaneh, for her love, support, and incredible patience, and my daughter, Shahrzad, for being there.

Table of Contents

Abstract	iv
Acknowledgment	vi
Chapter 1. Introduction	1
1.1. Background	1
1.2. Thesis objective	3
1.3. Thesis outline	4
Chapter 2. Literature Review	5
2.1. Triboelectrification of powders	5
2.1.1. Basic concepts of triboelectrification	9
2.1.2. Electron transfer	10
2.1.3. Ion transfer	14
2.1.4. Material transfer	14
2.1.5. Mode of contact	15
2.1.6. Condenser charge transfer model	17
2.1.7. Charge relaxation model	19
2.1.8. Charge transfer model for repeated impacts	20
2.1.9. Tribocharging in particle-laden pipe flows	23
2.2. CFD modeling of particle-laden flows	24
2.2.1. Continuous phase and solid phase modeling	26
2.2.2. Phase coupling	27
2.2.3. Turbulent flow modeling	28
2.2.4. Anisotropic turbulence in wall-bounded flows	29
2.3. Application of Artificial Neural Network (ANN) in predicting particle-wall interactions	33
Chapter 3. Methodology	36
3.1. Particle-laden flow dynamics	36
3.1.1. Fluid phase modeling	36
3.1.2. Solid-phase modeling	38
3.1.3. Phase coupling	42
3.1.4. Geometry and mesh	42
3.1.5. Computation of particle-wall interactions	44
3.2. Prediction of particle-wall collision number using Artificial Neural Networks	45

3.2.1. Database generation	45
3.2.2. Data preprocessing	46
3.2.3. Network topology	47
3.2.4. Network training	47
3.2.5. Network testing	48
3.3. Modeling particle tribocharging.....	49
3.3.1. Experimental charge measurement	49
3.3.2. Tribocharge modeling.....	51
Chapter 4. Results and discussion	57
4.1. Continuous phase modeling	57
4.2. Number of released particles into the system	58
4.3. Influence of particle Stokes number on particle-wall interactions	61
4.4. Influence of particle size and density on particle-wall interactions	69
4.5. Influence of pipe diameter and length on particle-wall interactions.....	72
4.6. Influence of air velocity on particle-wall interactions	74
4.7. ANN model for predicting particle-wall interactions	76
4.7.1. Number of neurons in the hidden layer	76
4.7.2. Network testing and model validation	77
4.8. Tribocharging model.....	80
4.8.1. Experimental charge measurement results	80
4.8.2. Influence of particle wall interactions on tribocharging in laminar particle-laden flows	81
4.8.3. Influence of material on tribocharging.....	84
4.8.4. Application of the numerical model.....	86
Chapter 5. Conclusions.....	90
References	92

List of Figures

Figure 1. Schematic illustration of charge transfer during the contact process, adapted from S. Matsusaka et al., 2010.	11
Figure 2. The triboelectric series proposed by Zou et al. (2019). Error bars indicate the range within a standard deviation.....	13
Figure 3. Influence of contact angle on the effective contact area (S. Matsusaka et al., 2010).	16
<i>Figure 4. Schematic diagram of the condenser model, adapted from S. Matsusaka et al., 2010.</i>	18
Figure 5. The relationship of contact gap and gaseous potential breakdown limit in Paschen's law (Matsuyama and Yamamoto, 1997).....	20
Figure 6. Variation of accumulated charge on a sphere by repeated impacts (Matsusaka, Ghadiri and Masuda, 2000).	21
Figure 7. Balance of generated electric current (a) and the difference of charge-to-mass ratios at the inlet and outlet of the tribocharger pipe (b)(Matsusaka and Masuda, 2006). 24	
Figure 8. Comparing calculated particle-wall mean collision numbers using different mesh sizes with experimental results	44
Figure 9. Network topology	47
Figure 10. Experimental set up for powder tribocharging and charge measurements (Howard university).....	50
Figure 11. The velocity magnitude and streamlines of turbulent flow with $Re=2700$ (a) and turbulence time scale profile (b).....	58
Figure 12. Calculated mean collision numbers for different numbers of released particles. The error bars represent the standard deviation.....	61

Figure 13. Particle trajectories for low (a), intermediate (b), and high (c) Stokes numbers. The color of trajectory lines shows the velocity magnitude (m/s) of particles. The x-axis points in the streamwise direction, the z-axis in the wall-normal direction, and the y-axis in the spanwise direction. 63

Figure 14. Comparison of near the wall particle number densities for different values of particle size (Stokes number)..... 64

Figure 15. Evolution of particle number density in the near-wall region for low Stokes particles..... 66

Figure 16. Evolution of particle number density in the near-wall region for intermediate Stokes particles. 67

Figure 17. Evolution of particle number density in the near-wall region for high Stokes particles..... 69

Figure 18. Influence of particle size on particle-wall mean collision numbers. Particles were released into a 1-meter pipe with 4.76 mm inner diameter and the air velocity was 8.4 (m/s)..... 70

Figure 19. Comparing mean collision numbers of 100-micron particles with different densities. All particles assumed spherical particles released into a 1-meter pipe with 4.76 mm inner diameter and the air velocity was 8.4 (m/s)..... 71

Figure 20. Influence of pipe diameter on particle-wall mean collision number. In all cases particles were released into a 1-meter pipe with 8.4 (m/s) air velocity..... 72

Figure 21. Influence of pipe length on particle-wall interactions. In all cases particles were released into a pipe with 4.76 mm inner diameter and 8.4 (m/s) air velocity. 74

Figure 22. Influence of air velocity on particle-wall mean collision numbers. All calculations were accomplished for a single pipe length (1 m), and diameter (4.76 mm).. 75

Figure 23. Influence of number neurons in the second layer on network performance.....	76
Figure 24. Comparing mean collision numbers calculated with CFD and predictions of the neural network (a), performance plot of the model (b).....	78
Figure 25. The average performance of the neural network.....	79
Figure 26. Regression analysis chart.	80
Figure 27. Computed particle-wall mean collision numbers for different particle sizes released into a pipe with 1.5 (m) length and 4.76 (mm) inner diameter and 6.5 (m/s) air velocity (Reynolds = 1900).....	82
<i>Figure 28. a) Effect of particle size on mean collision number and charge to mass ratio, b) the correlation of experimental charge to mass ratios and particle-wall mean collision numbers.</i>	84
Figure 29. Correlation of experimentally measured charge-to-mass ratios with calculated contact potential difference for samples with different protein content percentages. Error bars address the deviation of charge measurements during multiple experimental runs.	85
Figure 30. Measured and simulated charge-to-mass ratios for different particle sizes. The pipe material is PTFE (l = 1.5 m, d = 4.76 mm) and particles are organic flour ($\rho = 1440 \text{ kgm}^{-3}$).....	86
Figure 31. Flowchart describing an algorithm for particle size characterization based on particle charge-to-mass.	89

List of Tables

Table 1. Application of tribocharging in different research fields.	7
Table 2. Model constants.....	38
Table 3. Specifications of used grids.....	43
Table 4. Network inputs and output.....	46
Table 5. Particle and wall mechanical properties.....	55
Table 6. The particle-wall mean collision numbers and computation times calculated for different numbers of released particles into the system.	60
Table 7. Density of materials used in simulations.....	71
Table 8. Experimental charge measurement results for yellow pea powder dispersed into a PTFE tribocharger tube (1.5 m length, and 4.76 mm inner diameter) using air (6.5 m/s velocity) as the carrier fluid.....	81

Nomenclature

C	Capacitance (F)
C_L	Lagrangian time scale coefficient
D	Diameter (m)
E	Young's modulus (Pa)
e	Elementary charge (C)
F	Force term (N)
f	Collision frequency
g	Gravitational acceleration ($m \cdot s^{-2}$)
I	Current (A)
k	Elasticity parameter (Pa^{-1})
k_c	Charging efficiency (-)
k_b	Space charge constant ($V \cdot C^{-1}$)
k_e	Image charge constant ($V \cdot C^{-1}$)
k_r	Charge relaxation constant (s^{-1})
m_p	Particle mass (kg)
n	Particle-wall collision number
n_0	Characteristic number of collisions
p	Pressure (Pa)
q_c	Particle charge (C)
q_0	Initial charge (C)
q_∞	Particle equilibrium charge (C)
S	Contact area (m^2)
u	Fluid mean velocity ($m \cdot s^{-1}$)
u_τ	Friction velocity ($m \cdot s^{-1}$)
V_c	Contact potential difference (V)
V_b	Space charge potential difference (V)
V_e	Image charge potential difference (V)
W_p	Mass flow rate ($kg \cdot S^{-1}$)
y^+	Wall distance
z_0	Critical gap (m)
ε	Dissipation rate ($m^2 \cdot s^{-3}$)
ε_0	Electric permittivity of vacuum ($F \cdot m^{-1}$)
ν	Poisson ratio
ρ	Particle density ($kg \cdot m^{-3}$)
σ	Fluid velocity fluctuation
τ	Time scale
τ_L	Lagrangian time scale
τ_p	Particle relaxation time (s)
τ_w	Wall shear stress ($N \cdot m^{-2}$)
μ	Kinematic viscosity (kg/ms)
μ_T	Turbulent viscosity
ϕ	Work function (eV)

Chapter 1. Introduction

During powder transport in particle-laden pipe flows, electrostatic charge buildup occurs on contact surfaces due to particle-wall collisions. This phenomenon is known as triboelectrification or "tribocharging". Powder tribocharging is often referred to as a destructive phenomenon in various industries due to its catastrophic consequences. Dust explosions triggering by electrostatic discharge during the powder handling process are examples of these unwanted implications resulting in tremendous economic complications for industries, specifically those dealing with powders. In the pharmaceutical industry, powder tribocharging during transport in particle-laden pipe flows results in wall-fouling leading to inconsistencies in final product dosage. Therefore, there is considerable global interest in understanding the triboelectrification of powders and investigating the parameters influencing this phenomenon to mitigate drawbacks and take advantage of its potential benefits.

1.1. Background

Tribocharging is the phenomenon of electric charge transfer between different materials after any kind of contacting process such as rolling, sliding, and impact (S Matsusaka *et al.*, 2010). Triboelectricity has been known since 600 B.C., when the Greeks observed that amber, when rubbed with silk, attracted small pieces of straw (Pai and Springett, 1993). In Ancient Greek, the word 'tribo' refers to rubbing, and 'electron' describes amber. Triboelectric charging has been noticed in numerous natural phenomena such as volcanic eruptions (Miura, Koyaguchi and Tanaka, 2002), the creation of geological patterns such as razorbacks on Mars (Shinbrot, Lamarche and Glasser, 2006), and triboelectrification in dust storms (Kamra, 1972).

From an industrial perspective, triboelectric charging has drawn substantial attention over the years due to its beneficial and hazardous effects on production lines. Dust explosion is a severe issue in industries dealing with powder transport in high

volumes. In Germany, at least one dust explosion occurs every day, and electrostatic discharge is the root cause of 10% of these explosions (Glor, 2003). Moreover, 70% of industrial disasters that occurred over the past 50 years in Japan were related to electrostatic discharge (Ohsawa, 2003). In the pharmaceutical industry, wall-fouling due to deposition of charged particles on the inner wall of conveying lines results in inconsistencies of final product dosage, leading to rejection by regulations and enormous economic loss (Wong, Kwok and Chan, 2015).

Electrostatic separation of different materials is a promising application taking the advantage of triboelectrification of particles in the laboratory and industrial scales. In the recycling industry, tribocharging has been used for electrostatic separation of plastics (Laurentie, Traoré and Dascalescu, 2013). The application of electrostatic separation for dry beneficiation of coal has been addressed (Dwari and Rao, 2007). A tribo-electrostatic separation method was developed for dry fractionation of protein- and carbohydrate-enriched particles in organic powders (Tabtabaei *et al.*, 2016).

Electrophotography also benefits from triboelectrification of toner (Schein, 1999). The toner includes thermoplastic particles ranges from 5 to 10 microns in diameter, which triboelectrically gain charge due to contact with carrier beads. Charged toner adheres to the image charge deposited on the paper with a corona discharge, and consequently, thermoplastic particles melt due to high temperature and create the copy.

Tribocharging mainly occurs where particles are transported, such as fluidized beds, dry powder mixing, pneumatic conveying systems, and particle-laden flows. In fluidized beds, triboelectrification is a function of particle size, bubble size, and gas velocity (Luo *et al.*, 2003). It was confirmed that adding large particles to fluidized beds does not influence electrostatic charge generation. Conversely, based on the number of small particles added to the fluidized bed, an increase or decrease in charge generation was observed (Yu *et al.*, 2010). In the dry powder mixing, particles repeatedly collide with each other, leading to triboelectric charging, which disturbs

the mixing process and should be controlled (Karner and Urbanetz, 2012). Researchers examined the influence of powder triboelectrification in pharmaceutical powder blending processes, and the feasibility of triboelectric charge measurement for probing the blending uniformity of pharmaceutical powders was confirmed (Hao *et al.*, 2013). Many researchers have studied electrostatic charge generation during particle transport in pneumatic conveying systems (Cangialosi *et al.*, 2006; Korevaar *et al.*, 2014; Schwindt *et al.*, 2017). The conveying air velocity was recognized as a critical parameter in particle tribocharging during transport in pneumatic lines. An increase in the air velocity results in a higher turbulent dispersion and more particle-wall interactions, leading to high triboelectrification in pneumatic conveying systems (Grosshans and Papalexandris, 2017). However, in higher air velocities, the magnitude of charge generated due to tribocharging is insignificant as particles have a shorter residence time in the conveying pipes (Cangialosi *et al.*, 2006). In pneumatic systems, triboelectrification is an obstacle and is tried to be prevented due to its adverse effects on powder flowability.

Overall, tribocharging is a fairly unknown phenomenon, and a better understanding of this phenomenon not only helps to prevent the drawbacks, such as the risk of fire explosion and wall-fouling but could also help to improve current powder handling processes and develop new applications such as powder characterization and online monitoring of powder constituents, which is the scope of this thesis.

1.2. Thesis objective

The objectives of this thesis are:

- Examining the influence of different parameters such as particles diameter and density, pipe diameter and length, and fluid velocity on the particle-wall interactions using Computational Fluid Dynamics (CFD) methods.
- Predicting the particle-wall mean collision numbers based on the gas and solid phase properties using a CFD-based artificial neural network.

- Numerical modeling of particle tribocharging in particle-laden pipe flows based on particle-wall collision numbers obtained through CFD and the experimental charge measurement results.
- Investigating the influence of particle size and protein content on the charging behavior of samples.
- Proposing a method for rapid quantification of protein content and particle size characterization based on the generated charge during tribocharging in particle-laden pipe flows.

1.3. Thesis outline

Chapter 1. In this chapter, the triboelectrification of particulate materials in various fields is described. The specific objectives of this study are addressed, and the chapter closes with the outline of this thesis.

Chapter 2. This chapter describes the concepts and theoretical background for particle tribocharging in particle-laden pipe flows. Different approaches for modeling particle tribocharging are discussed. Current numerical methods for simulation of two-phase flows, such as Eulerian-Eulerian and Eulerian-Lagrangian approaches, are compared. Finally, the application of artificial neural networks in predicting particle motion in particle-laden flows is discussed.

Chapter 3. In this chapter, numerical simulation of particle-laden flow in turbulent and laminar pipe flows is studied using COMSOL Multiphysics® (Version 5.5). The influence of various parameters such as particle diameter and density, air velocity, and pipe dimensions on the number of particle-wall interactions is elucidated. A neural network model for estimating the particle-wall collision numbers based on physical parameters of particles and flow is proposed in this chapter. A tribocharging model is proposed for predicting particle charge to mass ratios based on particle-wall mean collision numbers.

Chapter 4. This chapter is a summary of the results obtained in the previous chapter.

Chapter 2. Literature Review

2.1. Triboelectrification of powders

Powders play a vital role in different industries as raw materials, excipients, or final products (S Matsusaka *et al.*, 2010) and are likely to accumulate electrostatic charge via handling processes such as sieving, grinding, pouring, and conveying. Powder transport in gas-solid pipe flow is the major cause of powder charging in industries (Gibson, 1997). Various phenomena occur due to powder electrostatic charging during transport in conveying lines; for instance, pharmaceutical powders often acquire charge due to repeated impacts with the pipe wall during conveying operations. Tribocharging contributes to powder adhesion and cohesion, leading to inconsistent powder flow and non-uniform dosage of the final product (Rowley, 2001). According to tight regulations of the pharmaceutical industry, the acceptable content uniformity of final products has a narrow range. Therefore, if the active ingredient(s) variations do not meet the pharmacopeial standards, the final product will not qualify by regulations, and hundreds of thousands of dollars could be wasted (Wong, Kwok and Chan, 2015). Hence, control of powder electrostatic charging during transport in conveying lines is essential to certify that the final product is uniform and safe to use.

Dust explosion is a severe issue in industries dealing with powder transport in high volumes. Bulk powders are excessively charged during industrial applications, which increases the chance of an electrostatic discharge. Specifically, in fine powders where particles have large surface-to-volume ratios, the accumulated charge is high enough to ignite fires and cause massive explosions due to electrostatic discharge (Ohsawa, 2011). In Germany, at least one dust explosion occurs every day, and electrostatic discharge is the root cause of 10% of these explosions (Glor, 2003). Moreover, 70% of industrial disasters that occurred over the past 50 years in Japan were related to electrostatic discharge (Ohsawa, 2003).

On the positive side, several industries, such as electrostatic powder coating (Bailey, 1998), electrostatic separation (Tabtabaei *et al.*, 2019), powder flow rate determination (Matsusaka and Masuda, 2006), and electrophotography (Schein, 1999) relies on triboelectric charging. Table 1 reviews the application of tribocharging in other research fields such as electrostatic separation, triboelectric nanogenerators (TENG), pharmaceutical, and indoor air quality (IAQ).

The influence of different parameters such as powder mass loading, carrier gas velocity, and material of powder and pipes on the charging behavior of particles has been investigated through numerous experimental and numerical studies. Tanoue *et al.* (2001) conducted a numerical simulation of triboelectrification of particles in a gas-solids two-phase flow and addressed the influence of particle size, air velocity, and pipe diameter on the particle tribocharging and validated the results with experimental data. The static electrification of powders during transportation in pneumatic conveying and the correlation between the acquired charge and transportation velocity and distance is addressed in several studies (Nifuku and Katoh, 2003). Watano *et al.* (2003) compared numerical results achieved for particle electrification in a pneumatic conveying process with experimental results to study the effect of particle-wall collision velocity and the number of collisions on tribocharging.

Unfortunately, most experimental tribocharging studies are not convincing due to inconsistent results, and the large scatter of measurements has made it difficult to fully understand the tribocharging process. These inconsistencies are attributed to various challenging factors that are difficult to control in experiments, such as environmental conditions and powder boundary conditions such as electric charging of samples during handling process of powders before feeding into an experimental charge measurement facility. Moreover, the non-uniformity of charge distribution on particles' surfaces leads to complications in electrostatic charge estimation and control (Matsusaka *et al.*, 2002).

The influence of environmental conditions on the tribocharging process was elucidated by experimental investigations by Schwindt *et al.* (2017), who studied the accumulation of static electricity during powder transport in a test rig that facilitated a high degree control of ambient conditions via a climate chamber. They confirmed that controlling ambient conditions enhance the reproducibility of experimental charge measurement results.

Some researchers investigated the influence of initial conditions such as particles' initial charge on charge transfer. They measured particle charge before and after impact on a wall and confirmed that the charge exchange between contact bodies strongly depends on the initial charge of particles before the impact (Yamamoto and Scarlett, 1986). It was also observed that along with the initial charge of particles, charge distribution on the surface of the particles also plays a vital role in charge exchange (Matsuyama *et al.*, 2003). Generally, powder handling before running experiments often results in unintended electric charging of sample powders, often overlooked by researchers, which could explain the large scatter of results observed in different experimental charge measurements.

Understanding the powder tribocharging process not only helps to prevent the drawbacks, such as the risk of fire explosion and wall-fouling in different industries but could also improve current powder handling processes and develop new applications such as powder characterization and online monitoring of powder constituents, which is the focus of this research.

Table 1. Application of tribocharging in different research fields.

Application	Research objective	Results	Reference
Electrostatic separation	Developing a novel solvent-free triboelectrification-based method for production of protein-enriched fractions from navy bean flour	The protein content of navy bean flour was increased by 22% after triboelectric separation.	(Tabtabaei et al., 2016)
	Investigating the impact of electric field strength and flow rate on triboelectric separation of a starch-protein mixture	Different gas flow rates in the charging tube did not change the separation	(Landauer & Foerst, 2018)

		characteristics, but increasing electrical field strength increased the separation efficiency of protein particles.	
	Developing a new system for mineral separation by providing the required electric potential to the electrodes of a separator using triboelectric charging.	The results showed that static electric charge could be increased to a maximum of ± 35 kV on an electrode by tribocharging. Furthermore, the separation test results revealed that non-conductive and conductive particles could be separated in an electrostatic separator using the high voltage directly produced by tribocharging.	(Dizdar et al., 2018)
	Assessing the effectiveness of aluminum- and polypropylene- made tribocharging chamber on electrostatic separation of polyethylene/polyvinyl chloride mixture	Aluminum and P.P. were found to be equally effective for the tribo electrostatic separation of the 50% PVC 50% P.E. sample. For the other two samples (10% PVC 90% PE, 90% PVC 10% P.E.), the best results were obtained with the P.P. tribocharging chamber.	(Calin et al., 2008)
	Electrostatic separation of polyethylene and polyvinylchloride after tribocharging	The average recovered content of the P.E. fractions was $> 90\%$ at a mass yield of $> 60\%$. The average recovered content of PVC was $> 40\%$, with an average mass yield of $> 30\%$	(Yanar & Kwetkus, 1995)
	Investigating the effect of triboelectric charging time and electric-field strength on the separation efficiency of polyvinylchloride (PVC) and polyethylene terephthalate (PET), using a separator consisting of a vibratory conveyor equipped with two plate electrodes	High purity and recovery of PVC and PET was obtained. The separation efficiency depends on the triboelectric charging time and electric-field strength.	(Saeki, 2006)
	Triboelectric belt separator for beneficiation of fine minerals	Triboelectric belt separator is ideally suited for separation of very fine ($< 1 \mu\text{m}$) to moderately coarse ($300 \mu\text{m}$) materials with very high throughputs.	(Bittner et al., 2014)
Triboelectric nanogenerators (TENG)	Developing a galloping triboelectric nanogenerator (GTENG) based on contact electrification between two flexible beams for energy harvesting under low wind speed.	The GTENG achieved an output voltage of over 200V at a low wind speed of 1.4 m/s	
	Proposing a multi-plate triboelectric nanogenerator for harvesting hydro energy	The maximum output power of this nanogenerator was	(Yin et al., 2019)

		about 225 μ W, which can lighten 106 LEDs at a water flow rate of 55L/min.	
Pharmaceutical	Investigating the effect of tribocharging behavior of pharmaceutical granules on the drying process in a fluidized bed dryer.	The research indicates that the amount of triboelectric charge is directly indicative of moisture content in the fluidized bed dryer, and monitoring its dynamic changes could be used to monitor the drying process in the pharmaceutical industry.	(Taghavivand et al., 2017)
	Understanding the triboelectrification of binary mixtures of drug and excipient	The electrostatic model suggests the inter-particle charge transfer is dominant and the drug particles charge positively at higher excipient:drug ratios in the blends	(Naik et al., 2016)
Indoor air quality	Developing two new electrostatic techniques for controlling domestic dust and allergenic particles in the domestic environment by tribocharging.	1. Electrostatically charged sprays removed up to 45% of the total mass of airborne dust particles. 2. Using charged powder applied to carpets results in dust removal of up to 99%, 15% more than when no powder was applied.	(Gaunt et al., 2003)
	Development and application of triboelectrically charged nonwoven electrets for air filtration.	The nonwoven electret media showed higher filtration efficiency compared to the uncharged media.	(Das & Waychal, 2016)

2.1.1. Basic concepts of triboelectrification

Tribocharging is the phenomenon of electric charge transfer between different materials after any kind of contacting process such as rolling, sliding, and impact (S Matsusaka *et al.*, 2010). Triboelectricity has been known since 600 B.C., when the Greeks observed that amber, when rubbed with silk, attracted small pieces of straw (Pai and Springett, 1993). In Ancient Greek, the word 'tribo' refers to rubbing, and 'electron' describes amber. Although triboelectricity has been studied for more than 2500 years, many aspects of this phenomenon remain unknown due to its complexity. There is still no compromise in the literature on the factor responsible for the charge transfer (S Matsusaka *et al.*, 2010). While most researchers acknowledge electron transfer as the primary charge transfer mechanism (Bailey, 1984; Shirakawa *et al.*,

2010), others believe in ion transfer (Diaz and Fenzel-Alexander, 1993; McCarty, Winkleman and Whitesides, 2007). The material transfer was first introduced as a charge transfer mechanism when it was observed that the impact between two bodies could result in a transfer of material fragments or surface impurities, and charge transfer occurs between contact bodies via these charged fragments (Robins, Lowell and Rose-Innes, 1980).

2.1.2. Electron transfer

Many researchers have addressed the fundamental of the charge transfer mechanism (Robins, Lowell and Rose-Innes, 1980; Bailey, 1984; S. Matsusaka *et al.*, 2010). Electron transfer is the most recognized charge transfer model for metal-metal contacts and has subsequently been used to describe metal-insulator contacts (Wong, Kwok and Chan, 2015). According to this model, electrons are transferred from a surface with a lower work function to a surface with a higher work function. The work function is the amount of energy required to take away an electron from the surface of a material and is strongly affected by the chemical composition of the surface. Electron transfer continues until two surfaces reach a uniform electron energy level (Bailey, 1984). At the separation moment, each contact surface gets an equal magnitude of charge with the opposite polarity (Figure 1). The contact potential difference between the contact surfaces, V_c is given by

$$V_c = \frac{(\phi_1 - \phi_2)}{e} \quad (2.1)$$

where ϕ_1 and ϕ_2 are the work functions of contact surfaces, and e is the elementary charge (Matsusaka and Masuda, 2003). The amount of the net charge transferred between contact surfaces, Δq , is estimated by the following equation

$$\Delta q = CV_c \quad (2.1)$$

where C is the capacitance between the contact bodies and depends on the contact area of surfaces and the charge cut-off distance at which no charge transfer occurs.

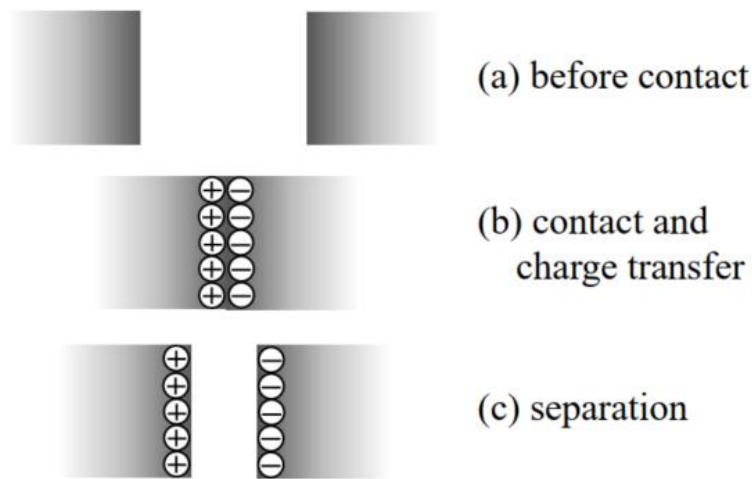


Figure 1. Schematic illustration of charge transfer during the contact process, adapted from S. Matsusaka et al., 2010.

Triboelectric series is a ranking table that categorizes materials according to the work function and could be used to predict the net charge and the relative charge polarity of contact surfaces. Electrons transfer from higher placed materials to materials in a lower position at the contact time based on triboelectric series. Therefore, higher positioned materials in triboelectric series are likely to charge positively, whereas materials in lower positions demonstrate negative charge. The triboelectric series has been frequently revised over time (Coehn, 1898; Hersh, Sharman and Montgomery, 1954; Henniker, 1962). Unfortunately, the consistency of this ranking profoundly depends on the experimental conditions (Gallo, Lama and Lama, 1976). Hence,

researchers struggled to achieve a trustworthy ranking by combining different qualitative triboelectric series from literature reports (Diaz and Felix-Navarro, 2004).

Zou *et al.* (2019) announced a universal standard method to establish a reliable triboelectric series for a wide range of polymers. The surface triboelectrification of tested materials was considered using liquid metal mercury as the reference material under well-defined environmental conditions. Figure 2 shows the triboelectric order of over 50 materials measured by this method.

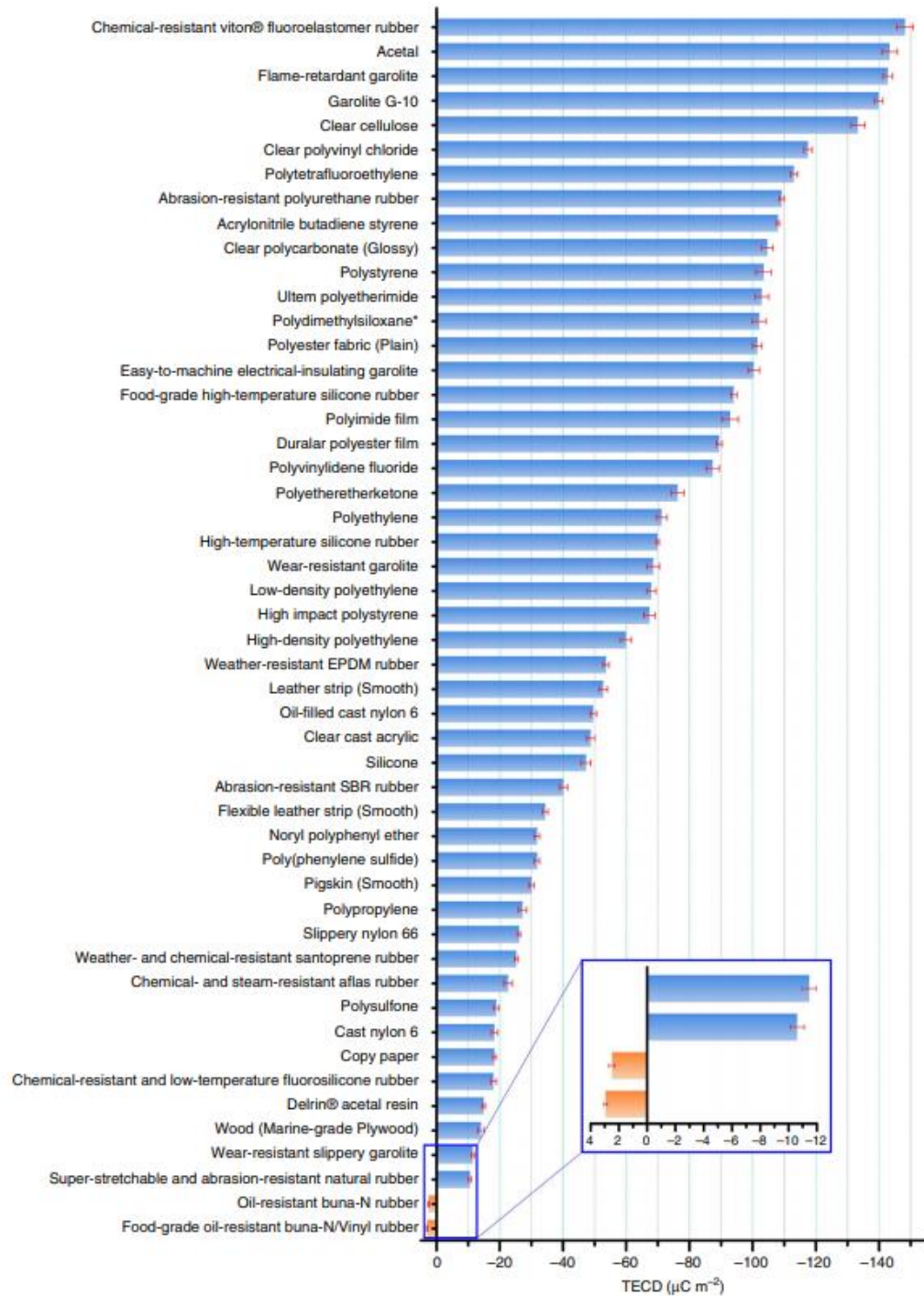


Figure 2. The triboelectric series proposed by Zou et al. (2019). Error bars indicate the range within a standard deviation.

2.1.3. Ion transfer

There is a general agreement on the charging mechanism of metals and semiconductors, but insulators' charging mechanism is less understood. The electron transfer model and other extensions of this model were used to elaborate the charge transfer between metals and semiconductors. However, electron transfer models consider the charge as a point charge and do not consider the chemical composition of the materials in the charging mechanism (Diaz, 1998). The first researches on insulators' contact charging mechanism, specifically polymers, were related to investigating the charging behavior of "toners" utilized in electrophotography. These studies confirmed that the chemical structure of the ions on the surface of polymers (toners) determines the sign and magnitude of the charge on them. These results proposed that an ion transfer model can correctly describe the charging mechanism on polymers containing ions, and there is no need to use electron transfer models (Diaz, 1998). According to the ion transfer model, a particle containing an immobile cation and a mobile anion will transfer the anion to the contacted surface, and consequently, the contacted surface develops a negative charge, and the particle develops a positive charge due to excess cations. Therefore, there would be no or little charge transfer in the absence of mobile ions on particles and contact surfaces (Diaz and Fenzel-Alexander, 1993).

2.1.4. Material transfer

During contact, a certain amount of material is likely to transfer from one surface to another surface. Bonds are broken during the separation of material from the main bodies. Therefore, these nanometer-sized fragments are considered charged and contribute to charge transfer during tribocharging (Lacks and Mohan Sankaran, 2011). The direction of material transfer between contact surfaces depends on the relative softness of contact bodies. Experimental results achieved through spectroscopic methods have confirmed charge transfer via material transfer during contact (Baytekin et al., 2011).

2.1.5. Mode of contact

Three types of contact are defined between contact surfaces during the charge transfer process: sliding, rolling, and collision. Although the term tribocharging encompasses all these contact modes, the charging characteristic of each mode is divergent, resulting in different ultimate charges of contact surfaces. Hence, it is essential to understand how different types of contact affect triboelectrification.

During the sliding process, charge transfer occurs due to friction at the contact interface. It is confirmed that the potential generated between contact surfaces during tribocharging is a function of the surface material friction coefficient (Jing *et al.*, 2014). Material transfer due to sliding friction between surfaces results in changing the original surface compositions, altering the contact surfaces' work functions and friction coefficients, consequently affecting the tribocharging process (Chang, Chu and Chou, 2007).

In rolling contact mode, particles roll over the wall, and the contacting surface is much larger. On the other hand, the friction coefficient between surfaces is lower compared to the sliding mode. During rolling contact mode, the charge transfer process could not be justified by the well-known condenser model as the contact surfaces are not identical to the plates of a capacitor. Therefore, the charge accumulation on particles rolling on a flat surface is modeled based on the contact area of rolling particles and the contact time (Ireland, 2010). Moreover, the tilt angle of the target wall essentially influences the contact area and charging process during the rolling mode. Ema *et al.* (2003) investigated the influence of contact angle (θ) on tribocharging of particles. They explained their experimental results by a rolling-slipping model. It was observed that the contact area increases for $\theta \leq 60^\circ$ (Figure 3a) due to the rolling of particles on the wall, and tribocharging is enhanced sequentially. Whereas, for $\theta > 60^\circ$ (Figure 3b), the contact area decreases as the slipping pattern became the dominant contact mode resulting in less efficient tribocharging.

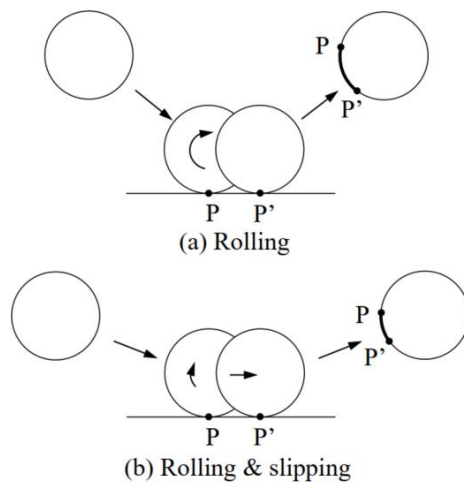


Figure 3. Influence of contact angle on the effective contact area (S. Matsusaka *et al.*, 2010).

Collision or impaction mode is the most effective contact process during tribocharging. The collision force generated at the interface in this mode is far more significant than the forces generated during the sliding and rolling process. The efficiency of tribocharging due to particle-wall collisions is firmly influenced by the elastic properties of contact surfaces affecting the contacting area (Thornton, 1997). Moreover, it was observed that in addition to the elastic properties of contact surfaces, the particle shape and surface roughness also affected the contact area during collisions (Watanabe *et al.*, 2007). The surface roughness of contact bodies and the irregularities in particle shape result in contact area alterations during each collision leading to the high variation of measured charge during experimental tribocharging studies. Overall, tribocharging is a surface-physics phenomenon that significantly depends on contact surfaces' physical and chemical properties.

In the next section of this chapter, different charge transfer models developed for describing electron transfer between contact bodies are discussed.

2.1.6. Condenser charge transfer model

The condenser model describes the electron transfer process between contact surfaces in terms of a capacitor. The contact surfaces are considered the plates of a capacitor in which charge transfer occurs due to the potential difference between the two plates. Figure 4 illustrates the condenser model for charge transfer during contact. According to the condenser model, the transferred charge caused by particle impact on a wall, Δq , is given by (Matsusaka, Ghadiri and Masuda, 2000)

$$\Delta q = k_c CV, \quad (2.2)$$

where k_c is the charging efficiency, C is the capacitance between the two materials, and V , is the total potential difference between contact surfaces. The capacitance between contact surfaces is given by

$$C = \frac{\epsilon_0 S}{z_0} \quad (2.3)$$

where ϵ_0 is the permittivity of carrier gas, S is the contact area between contact bodies, and z_0 is the critical gap between surfaces which depends on the surface roughness and geometry of surfaces. The total potential difference, V , between contact surfaces is given by

$$V = V_c - V_e - V_b + V_{ex} \quad (2.4)$$

where V_c is the potential difference based on the work function of contact materials and is calculated by equation 2.1. V_e , is the potential difference come from the image charge, and is given by

$$V_e = k_e q \quad (2.5)$$

where k_e is the image charge efficiency, and q is the charge carried on the particle before contact. When the electric field from a point charge induces a charge on its surrounding, it is called image charge. V_b is the potential difference produced by neighboring charged particles, which is known as space charge and is given by

$$V_b = k_b q \quad (2.6)$$

Space charge happens when several point charges perform together to establish a cloud of charge. Finally, V_{ex} is the potential difference triggered by external electric fields.

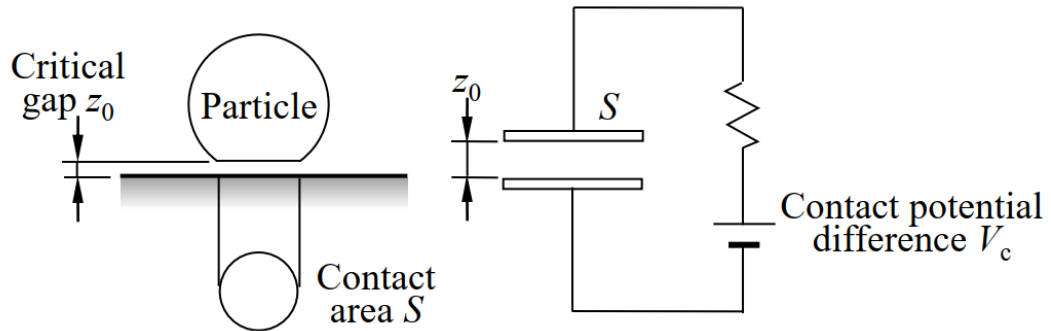


Figure 4. Schematic diagram of the condenser model, adapted from S. Matsusaka et al., 2010.

2.1.7. Charge relaxation model

After the collision in the tribocharging process, the contact surfaces initiate a separation process from each other, and consequently, the gap between surfaces is filled by the surrounding gas. The capacitance of contact surfaces is inversely related to the distance between them. Therefore, during separation, the capacitance reduces by the gap distance. Based on the condenser model, the amount of charge maintained on the surfaces is a function of capacitance and the potential difference. Since the amount of charge on contact surfaces is constant, the total potential difference between these two surfaces increases instantly with increasing the gap distance during the separation process (Matsuyama and Yamamoto, 1995). When the potential difference between surfaces surpasses the gaseous breakdown limit, the charge relaxation occurs.

The Paschen curve is applied to determine the gas breakdown limit between surfaces (Paschen, 1889). The Paschen curve illustrated in Figure 5 describes the correlation between the distance of the contact surfaces and the potential breakdown limit between them. When a particle with a nominal initial charge approaches a wall, charge transfer occurs due to contact. If the amount of transferred charge is high enough to cause an intersection between the Paschen curve and the potential curve, the charge relaxation occurs, and the potential curve leaves the Paschen curve with a lower level of potential. Accordingly, the total remaining charge on the particle is more significant compared to the initial charge. Conversely, if the amount of initial charge is significant on the approaching particle, the potential curve intersects with the Paschen curve before impact, and due to the gas break down, the particle releases the extra charge. However, the remaining charge on the particle is preserved after contact because the potential curve of the particle does not intersect with the Paschen curve.

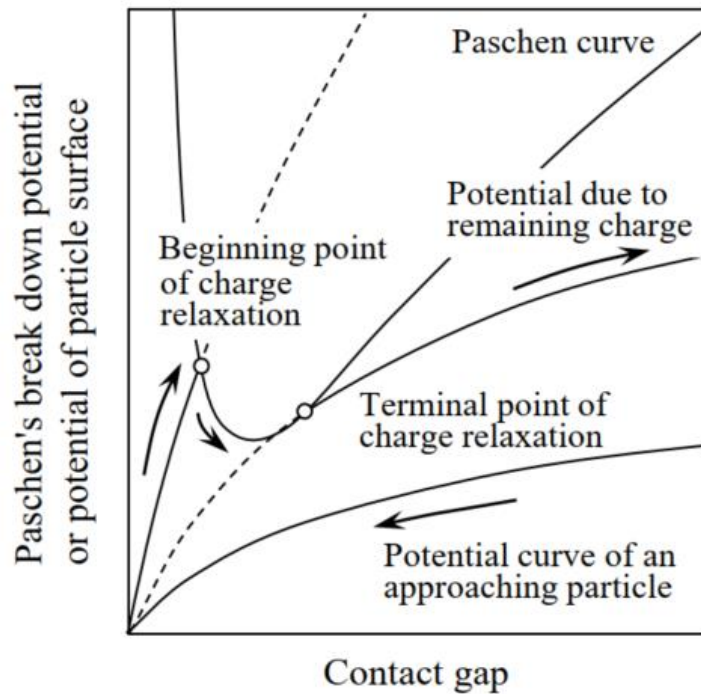


Figure 5. The relationship of contact gap and gaseous potential breakdown limit in Paschen's law (Matsuyama and Yamamoto, 1997).

2.1.8. Charge transfer model for repeated impacts

In particle-laden flows, particles repeatedly collide with the channel wall, and charge transfer occurs. Since the boundary conditions such as the initial charge on particles and the state of the collisions before every collision are different, it is essential to monitor the particle's charge variation during transport in particle-laden flows. Therefore, Matsusaka and the research team studied the charge accumulation on particles due to repeated impacts on a wall (Matsusaka, Ghadiri and Masuda, 2000). They used a large sphere with 31 mm in diameter attached to a fine string to control the collisions with the wall. The sphere was made of synthetic rubber. The sphere was dropped onto the plate, pulled up using the attached string, and dropped again at different intervals. The initial charge of the sphere and the transferred charge were measured before and after each collision using a Faraday cage. Figure 6 shows the

variation of the sphere accumulated charge based on the number of impacts with different intervals between impacts. It can be observed from the graph that the accumulated charge of the sphere increases with the number of collisions and approaches a limiting value. Moreover, the accumulated charge will likely decrease by increasing the time interval between collisions, contributing to electrostatic charge leakage.

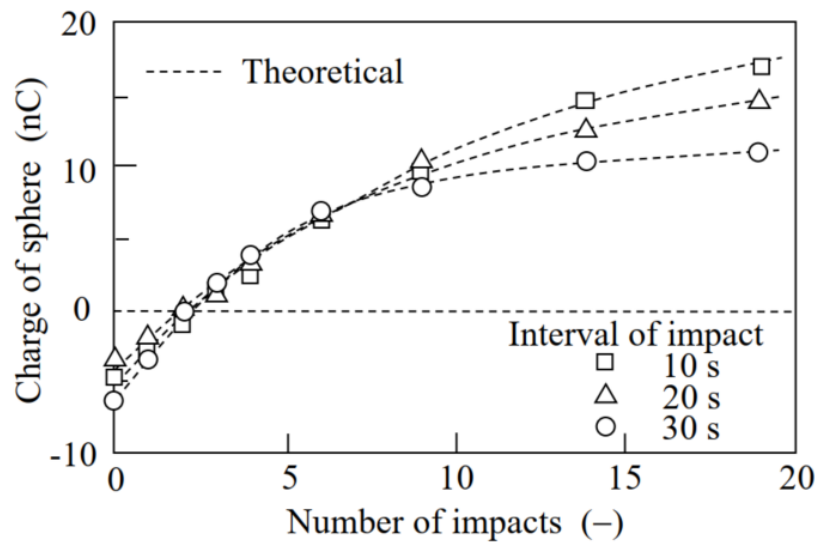


Figure 6. Variation of accumulated charge on a sphere by repeated impacts (Matsusaka, Ghadiri and Masuda, 2000).

To acquire the charge of a particle (q_c) as a function of the number of contacts with a wall (n), a continuous quantity (dq_c/dn) could be defined based on the condenser model

$$\frac{dq_c}{dn} = k_c CV, \quad (2.7)$$

The electrostatic charge leakage significantly affects the final charge of particles after collisions. The charge leakage is triggered by the redistribution of charge on the particle surface and is approximated by (Itakura *et al.*, 1996)

$$\frac{dq_r}{dn} = -\frac{k_r}{f} q, \quad (2.8)$$

where k_r is a constant related to the effect of charge leakage, and f is the frequency of particle collisions. Therefore, the total charge transfer (dq/dn) is given by

$$\frac{dq}{dn} = \frac{dq_c}{dn} + \frac{dq_r}{dn} = -\alpha q + \beta, \quad (2.9)$$

where α is a constant contributes to the effects of charge relaxation, image charge, and space charge, and β accounts for the effect of external electric fields and work functions.

Finally, assuming the initial conditions, $n = 0$ and $q = q_0$, the total charge of particle could be approximated by the following exponential equation

$$q = q_0 \exp\left(-\frac{n}{n_0}\right) + q_\infty \left\{1 - \exp\left(-\frac{n}{n_0}\right)\right\}. \quad (2.10)$$

where q_0 is the initial particle charge, q_∞ is the particle equilibrium charge, and n_0 is the characteristic number of collisions associated with the particle-wall system.

2.1.9. Tribocharging in particle-laden pipe flows

In particle-laden pipe flows, charge transfer occurs due to continuous particle-wall interactions. In the dilute phase, particles repeatedly collide with the pipe wall due to negligible inter-particle collisions, enhancing charge transfer efficiency. In the dense phase, particle-particle interactions reduce the chance of charge transfer through particle-wall collisions (S Matsusaka et al., 2010). It was confirmed that in dilute particle-laden flows, the electric current generated in pipes during charge transfer is proportional to the mass flow rate of particles in the system (Masuda *et al.*, 1998). Later, Matsusaka and coworkers observed that the value of generated current per unit mass flow rate equals the transferred charge-to-mass ratio of particles (Matsusaka *et al.*, 2008). They measured the charge-to-mass ratio of particles at the inlet and outlet of the tribocharger pipe using a Faraday cup, and the generated current in the pipe was measured using an oscilloscope simultaneously. Results are described in Figure 7, indicating that the current per unit mass flow rate (I/W_p) generated in the system is equal to the difference of charge-to-mass ratios at the inlet and outlet of the pipe ($q_{mIN} - q_{mOUT}$). They proposed that the amount of transferred charge between particles and the wall could be approximated by the generated electric currents using the following equation

$$\begin{aligned} \frac{I}{W_p} &= -\frac{\Delta q}{m_p} \\ &= (q_{m0} - q_{m\infty}) \left\{ \exp\left(-\frac{n(x)}{n_0}\right) \right\} \left\{ 1 - \exp\left(-\frac{n(\Delta x)}{n_0}\right) \right\}. \end{aligned} \tag{2.11}$$

where W_p and m_p are the mass flow rate and total mass of particles, respectively. q_{m0} is the initial charge-to-mass ratio of particles at the inlet ($x=0$), and $q_{m\infty}$ is the specific charge-to-mass ratio of particles after traveling the pipe length (Δx).

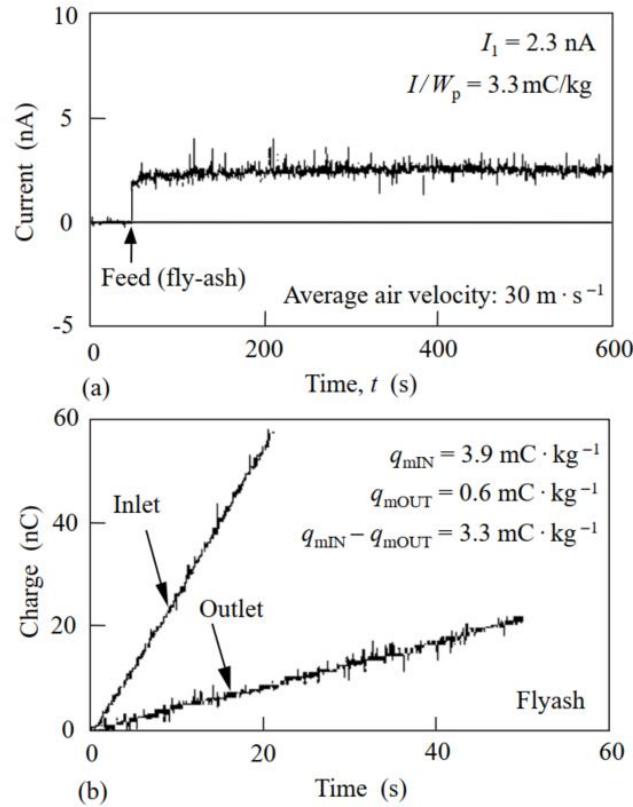


Figure 7. Balance of generated electric current (a) and the difference of charge-to-mass ratios at the inlet and outlet of the tribocharger pipe (b)(Matsusaka and Masuda, 2006).

2.2. CFD modeling of particle-laden flows

Particle transport in wall-bounded flows has many applications in different fields of engineering. Measuring and predicting the particle-wall collision frequency is essential in various areas of engineering such as pneumatic conveying, powder transport, pipes wear erosion, and powder tribocharging. This study is motivated by particle-wall interactions of solid, dense particles in smooth wall-bounded turbulent

and laminar pipe flows. The target here is estimating the number of particle-wall collisions under different boundary conditions for modeling particle tribocharging in chapter 3 of this thesis.

Tsuji and Morikawa (1987) performed a numerical simulation of gas-solid two-phase flow to study the particle trajectories in a two-dimensional horizontal channel. The gas-phase was simulated using a finite-difference method, and particle trajectories were calculated using the Lagrangian approach. The experimental results achieved through a horizontal channel flow were used to validate the simulation results. Yamamoto (2001) performed the numerical simulation of particle transport in a turbulent vertical channel to investigate the interaction between fluid turbulence and particle motion. Large-eddy simulation (LES) and Lagrangian methods were utilized to solve the fluid and solid phases. They confirmed that inter-particle collisions impact the motion of high-inertia particles near the channel wall and small-inertia particles at the center of the channel. For the first time, Sommerfeld and Huber (1999) considered the influence of wall roughness and particle shape on the particle-wall collision process. They used various particle and wall materials in their experiments to modify a Lagrangian model which can solve particle trajectories with high accuracy. They explained that wall roughness increases wall collision frequency by enhancing the irregular particle bouncing. An Eulerian-Lagrangian model was developed for the characterization of turbulent gas-solid flows in pipe systems (Huber and Sommerfeld, 1998). The influence of turbulent structures, wall roughness, and particle-particle collisions on gas-solid flows was investigated in pipes with different materials. Phase Doppler anemometry was utilized for validating numerical simulation results. Uijttewaala and Oliemans (1996) studied the motion of particles in a turbulent gas flow using direct numerical simulation (DNS) and Large Eddy Simulation (LES) for the single-phase pipe flow and Lagrangian approach for the particle phase. They concluded that small particles are susceptible to the turbulent fluctuations that occur in near-wall regions. At the same time, the motion of large particles is more affected by the overall turbulent characteristics than near-wall turbulence fluctuations.

Generally, particles' inertia and fluid's turbulent structures affect particles' motion, consequently governing particle-wall interactions (Young and Leeming, 1997). Chan *et al.* (2020) defined three different particle transport regimes based on direct numerical simulation of particles with various Stokes numbers in a turbulent pipe flow. At a very low Stokes regime, particles' motion is entirely governed by the turbulent structures, and particles act like tracers that follow fluid streamlines. The transport of particles with very large Stokes numbers is not affected by turbulent fluctuations. Inertia and mass forces such as gravity influence the motion of particles in the high Stokes regime. At the intermediate Stokes regime, particles' motion is governed by both turbulent structures and particle inertia.

2.2.1. Continuous phase and solid phase modeling

The CFD models for simulating gas-solids flows are grouped into two main categories according to how the solid phase is treated; Eulerian-Lagrangian, and Eulerian-Eulerian models. In Eulerian-Lagrangian models, the fluid is modeled in the Eulerian cell-based framework through the solution of mass and momentum conservation equations. In contrast, the movement of the solid phase is determined by solving the equation of motion for a certain number of computational particles (Curtis and Van Wachem, 2004). In Eulerian-Lagrangian models, the individual particles are tracked through the representation of their Lagrangian trajectories. In Eulerian-Eulerian models, both the fluid and the solid phases are described in the Eulerian cell-based framework through the solution of their mass and momentum conservation equations. Consequently, only a fictitious fluid representing the local behavior of the ensemble particles is modeled. For this reason, the Eulerian-Eulerian models are also referred to as two-fluid models (Capecelatro and Desjardins, 2013).

Several aspects should be considered to select the most appropriate modeling approach for a particle-laden flow system, such as the level of detail of the information required and the computational cost (Pai and Subramaniam, 2009). Eulerian-Lagrangian models are helpful to simulate phenomena occurring at the scale of

particles, such as, for instance, the material removal due to collisions between the particles and the solid surfaces, impact erosion, or charge transfer (Desjardins, Fox and Villedieu, 2008). Eulerian-Eulerian models are suitable to investigate processes governed by the particles as a whole, for instance, to predict the distribution of the solids and the frictional losses in pipelines (Gidaspow, 2012).

2.2.2. Phase coupling

The computational burden of Eulerian-Lagrangian models is strongly affected by the number of calculated trajectories and the number of particles in the flow (Patankar and Joseph, 2001). If the solid concentration is deficient, the one-way coupling regime occurs, in which the fluid flow field is not affected by the particles (Elghobashi, 1994). The fluid flow field is solved first, and then the particle trajectories are calculated sequentially. The computational burden of these simulations is generally low and increases proportionally to the number of computational particles (Capecelatro and Desjardins, 2013). In a two-way coupling regime, the particles also affect the fluid flow field (Elghobashi, 1991). Therefore, the fluid flow equations and the particle equations of motion are solved within a loop. After solving the fluid flow equations, the trajectories of the particles are calculated one by one, and the fluid flow equations are modified according to the calculated trajectories, and the whole loop is repeated.

Consequently, the computational cost might be significant in a two-way coupling regime (Ferrante and Elghobashi, 2003). In a four-way coupling regime, also particle-particle interactions must be considered. In this regime, the particle trajectories are no longer calculated one by one but simultaneously (Laín, Sommerfeld and Kussin, 2002). The reason is that particles' trajectory is affected by other particles via inter-particle collisions (Crowe *et al.*, 2011). In this case, the computational burden becomes huge and generally unaffordable for complex flows.

In Eulerian-Eulerian models, mass and momentum conservation equations are solved for both phases in a coupled manner. This implies that the influence of the solids on the fluid flow is always accounted for, even when this effect is minimal (Kartushinsky

et al., 2016). Eulerian-Eulerian models are either two-way coupled or four-way coupled. Particle-particle interactions are modeled through the formulation of the momentum conservation equation of the solid phase. As a result, Eulerian-Eulerian models are computationally cheaper than Eulerian-Lagrangian models, and their computational burden is substantially unaffected by the coupling regime and the number of particles in the flow (Chiesa *et al.*, 2005). Practically, Eulerian-Eulerian models are the only CFD models applicable to dense particle-laden flows (Subramaniam, 2013).

2.2.3. Turbulent flow modeling

Most particle-laden flows of engineering interest are turbulent. Therefore, CFD models are also classified according to the approach to turbulence modeling. Turbulence develops across multiple scales, spanning from the integral scale (large eddies), to the Kolmogorov scale (small eddies). The direct numerical simulation models (DNS) involve the direct solution of Navier-Stokes equations and resolve all turbulence scales (Friedrich *et al.*, 2001). In large eddy simulation models (LES), all turbulence scales are resolved down to a certain level, and the more minor scales are modeled (Moin, 1997).

Generally, the most widely used engineering modelings are based on the Reynolds averaged Navier-Stokes (RANS) method due to their lower computational burden. RANS-based models resolve only the integral scale of the turbulence using the RANS equations, and all other turbulence scales are modeled (Kalitzin *et al.*, 2005). RANS-based Eulerian-Lagrangian models are a category of CFD models utilized to simulate turbulent particle-laden flows, which combine the Eulerian-Lagrangian approach to describe the motion of the two phases. RANS models allow solving the flow at the integral scale of turbulence. All other scales (Kolmogorov scale) are not resolved but indirectly accounted for via the turbulence model (Duraismy, Iaccarino and Xiao, 2019). The integral scale governs the required size of the computational mesh. The relatively coarse meshes required by RANS-based models cause a low computational

burden even for complex flows, explaining why RANS is the most widely used approach in engineering (Xiao and Cinnella, 2019).

Combining the standard k - ε turbulence model with Lagrangian particle tracing methods is relatively easy because of its fast convergence and low memory requirements (Lew, Buscaglia and Carrica, 2001). In addition, the k - ε turbulence model directly allocates degrees of freedom for k (turbulent kinetic energy) and ε (turbulent dissipation rate), which are essential for modeling the turbulent dispersion of particles accurately. The k - ε turbulence model introduces dependent variables and transport equations for the turbulent kinetic energy (k) and the turbulent dissipation rate (ε). The turbulent kinetic energy (SI unit: m^2/s^2) represents the energy per unit mass associated with eddies in the flow, and the turbulent dissipation rate (SI unit: m^2/s^3) indicates the rate at which turbulent kinetic energy in the eddies is converted to thermal energy. Using turbulent kinetic energy and turbulent dissipation rate makes it possible to define two new dependent variables, which provide an in-depth look at the size and lifetime of the eddies in the flow. The ratio of turbulent kinetic energy to turbulent dissipation rate (k/ε) indicates the average eddy lifetime, whereas the length scale (size) of the largest eddies in the flow is defined as $k^{3/2}/\varepsilon$. The terms turbulent kinetic energy and dissipation rate are used for solving the RANS equations.

2.2.4. Anisotropic turbulence in wall-bounded flows

Particle transport in homogeneous and isotropic turbulent flows has been widely studied by researchers (Squires and Eaton, 1991), whereas wall-bounded turbulent flows have not attracted the same attention. Turbulent in wall-bounded flows is inhomogeneous and anisotropic, making them more complicated than isotropic flows in modeling the random velocity fluctuations that affect particle trajectories during transport (Dehbi, 2008). In the Continuous Random Walk (CRW) model, the velocity perturbations are integrated over time, whereas in other models such as the Discrete Random Walk (DRW) model, unique velocity perturbations are added to the mean

velocity field at discrete times (Gosman and Ioannides, 1983). CRW models are based on the Langevin equation, and deliver more accurate predictions of turbulent particle dispersion than DRW models, especially in studies where inhomogeneous effects are significant (Dehbi, 2008).

The particle transport and dispersion in turbulent flows highly affected by the carrier fluid velocity fluctuations. The well-known Langevin equation has been used massively to describe the fluid velocity fluctuations continuously. This equation was first proposed by Langevin (1908) for modeling the Brownian motion of very small particles. Later, other researchers modified this equation for describing the fluid velocity fluctuations in homogeneous turbulence (Obukhov, 1959; Di Anibal, Callao and Ruisánchez, 2011). For a homogeneous isotropic turbulence flow, the classical Langevin equation is

$$du_i = -u_i(t) \frac{dt}{\tau_i} + \sigma_i \sqrt{\frac{2}{\tau_i}} d\xi_i, \quad (2.12)$$

The subscript i indicates the three components of the fluid velocity field, τ_i is a timescale, $d\xi_i$ is a succession of uncorrelated random numbers with zero mean, and σ is the RMS fluid velocity fluctuation with a similar value in any direction when the flow is assumed isotropic, and is given by

$$\sigma = \sigma_1 = \sigma_2 = \sigma_3 = \sqrt{\frac{2k}{3}}. \quad (2.13)$$

Where k is the turbulent kinetic energy. In wall-bounded flows like pipe flows, the turbulence becomes inhomogeneous as the turbulent kinetic energy is heavily

damped near the walls. Furthermore, as wall-bounded flows are anisotropic, the velocity component normal to the wall is more heavily damped than the velocity components in the streamwise and spanwise directions (Dehbi, 2008). Therefore, some corrections should be applied to the classic Langevin equation in the region $y^+ < 100$, where y^+ is the wall distance in viscous units,

$$y^+ = x_2 \frac{u_\tau}{\nu} \quad (2.14)$$

where x_2 (m) is the normal distance to the nearest wall, ν (m^2/s) is the fluid kinematic viscosity, and u_τ (m/s) is the friction velocity, and is given by

$$u_\tau = \frac{\tau_w}{\rho} \quad (2.15)$$

where τ_w (N/m^2) is the wall shear stress. The normalized Langevin equations in three different directions are as follows (Iliopoulos, Mito and Hanratty, 2003),

$$\begin{aligned} d\left(\frac{u_1}{\sigma_1}\right) &= -\left(\frac{u_1}{\sigma_1}\right) \frac{dt}{\tau_1} + \sqrt{\frac{2}{\tau_1}} d\xi_1 + \frac{\partial(\overline{u_1 u_2 / \sigma_1})}{\partial x_2} \frac{dt}{1 + Stk} \\ d\left(\frac{u_2}{\sigma_2}\right) &= -\left(\frac{u_2}{\sigma_2}\right) \frac{dt}{\tau_2} + \sqrt{\frac{2}{\tau_2}} d\xi_2 + \frac{\partial \sigma_2}{\partial x_2} \frac{dt}{1 + Stk} \end{aligned} \quad (2.16)$$

$$d\left(\frac{u_3}{\sigma_3}\right) = -\left(\frac{u_3}{\sigma_3}\right)\frac{dt}{3} + \sqrt{\frac{2}{\tau_3}}d\xi_3$$

where \mathbf{u}_1 , \mathbf{u}_2 , and \mathbf{u}_3 are the streamwise, wall-normal, and spanwise components of the turbulent velocity perturbation. The RMS fluid velocity fluctuations (σ_i) in anisotropic wall-bounded flows are obtained via DNS fits by (Dreeben and Pope, 1997),

$$\begin{aligned}\sigma_1^+ &= \frac{\sigma_1}{u_\tau} = \frac{0.40y^+}{1 + 0.0239(y^+)^{1.496}} \\ \sigma_2^+ &= \frac{\sigma_2}{u_\tau} = \frac{0.0116(y^+)^2}{1 + 0.0203y^+ + 0.00140(y^+)^{2.421}} \\ \sigma_3^+ &= \frac{\sigma_3}{u_\tau} = \frac{0.19y^+}{1 + 0.0361(y^+)^{1.322}}\end{aligned}\tag{2.17}$$

Bocksell and Loth (2006) proposed that the Lagrangian timescales are the same in all three directions (τ_1, τ_2, τ_3) and are equal to τ_L ,

$$\tau_L = \frac{C_L k}{\varepsilon}\tag{2.18}$$

where C_L is a dimensionless constant called the Lagrangian time scale coefficient, k is the turbulent kinetic energy, and ε is the turbulent dissipation rate.

The Lagrangian time scale in the anisotropic flow boundary layer is approximately the same in all directions but calculated differently. The following polynomial fit for the time scale is proposed by Kallio and Reeks (1989).

$$\begin{aligned} \tau_L^+ &= \tau_L \frac{u_\tau^2}{\nu} \\ &= \begin{cases} 10 & y^+ < 5 \\ 7.122 + 0.5731y^+ - 0.00129(y^+)^2 & 5 \leq y^+ \leq 100 \end{cases} \end{aligned} \quad (2.19)$$

where ν (m²/s) is the fluid kinematic viscosity.

2.3. Application of Artificial Neural Network (ANN) in predicting particle-wall interactions

Particle transport in particle-laden flows is affected by various parameters related to the solid phase properties (particle size, density, shape) or the conveying line properties (gas velocity, gas pressure, pipe geometry). A novel idea to predict particle-wall collision numbers in particle-laden flows is to use artificial neural networks (ANN). Latest advances in artificial neural networks have offered a potent tool for analyzing non-linear systems, such as particle-laden flows. ANNs are competent in learning the complicated correlations between various variables by assigning weights and biases attached to the neurons (Clarkson, 1996).

ANN is widely used in various fields such as turbulence modeling (Gamahara and Hattori, 2017; Duraisamy, Iaccarino and Xiao, 2019), predicting particle trajectories in turbulent flows (Grossi, Kubat and Özgökmen, 2020), flow regime identification (Mi, Ishii and Tsoukalas, 2001), and friction factor prediction (Yuhong and Wenxin, 2009). The hydrodynamic behavior of particle motion in a three-phased fluidized bed

was modeled using an artificial neural network (Otaawara *et al.*, 2002). Pandya *et al.* (2017) developed a CFD-based artificial neural network model to estimate solid particle erosion due to particle-wall interactions in gas-solid pipe flows. They performed a statistical analysis based on output parameters obtained through CFD to investigate the influence of various parameters on particle erosion rates. They achieved a 25% improvement in estimating cumulative erosion rate error compared to a standard erosion model. Gheziel *et al.* (2021) presented an ANN model to explain particle distribution concentration in indoor air with some input variables such as particle size and flow velocity. The performance of the presented model was validated by experimental results and results determined by the CFD model. Electrostatic sensing and neural network techniques were integrated for velocity and mass flow rate measurement of particles in pneumatic conveying lines (Yan, Xu and Lee, 2006). Results confirmed that this approach could offer a cost-effective method for complex flow measurement issues.

Determining the appropriate network topology for a specific problem is an actual step influencing network performance and liability. Therefore, an exemplary network architecture requires high expertise in identifying proper hyperparameters for the network, such as the number of hidden layers, the number of neurons in each layer, and a knowledgeable background in the corresponding field (Anochi and De Campos Velho, 2015). Hence, this topic has been the subject of enormous research in recent years (Ghanou and Bencheikh, 2016; Ramchoun *et al.*, 2016).

In the next chapter, the tribocharging model used for modeling the charging behavior of particles in a particle-laden flow and the experimental charge measurement results used for model validation are discussed. Further, a detailed description of the CFD model developed for simulating the hydrodynamic behavior of particles in a particle-laden flow and calculating the particle-wall collision numbers is presented. Finally, the process of training a neural network based on the CFD results is explained for

predicting particle-wall mean collision numbers based on various input parameters such as air velocity, particle size, particle density, and pipe dimensions.

Chapter 3. Methodology

3.1. Particle-laden flow dynamics

The particle-laden flow system studied in this thesis comprises of spherical particles transported by incompressible air as the carrier fluid. Reynolds Averaged Navier-Stokes (RANS) equations were used for modeling the particle-laden flow and the standard k- ϵ method was used for turbulence modeling. To solve the RANS equations, the Eulerian framework was used for the gas phase, and the solid phase was solved using the Lagrangian framework. The particle-laden flow was assumed to be in the dilute phase, which means that the volume fraction of the solid phase is very low compared to the volume fraction of fluid phase. One-way coupling was used in this study, which means that the influence of particles on fluid flow and the interparticle interactions are not considered. COMSOL Multiphysics® (version 5.5) was used for simulating particle trajectories in a particle-laden flow.

The following sections will describe the fluid phase and solid phase dynamics, followed by the coupling method used for the two phases. The computation process of counting particle-wall interactions is also presented in this chapter.

3.1.1. Fluid phase modeling

In this study, a RANS-based Eulerian-Lagrangian model was used to determine particle trajectories in turbulent gas-solids pipe flow. The turbulent channel flow is modeled using RANS equations, and the fluid velocity is defined as the sum of a deterministic mean flow term and a random velocity perturbation, representing the eddies.

The RANS equations for a stationary, incompressible flow are

$$\rho(u \cdot \nabla)u = \nabla \cdot [-pI + (\mu + \mu_T)(\nabla u + (\nabla u)^T)] + F, \quad (3.1)$$

$$\rho \nabla \cdot \mathbf{U} = 0$$

where \mathbf{u} is the fluid velocity vector, p is the pressure, and ρ is the fluid density. μ and μ_T are the kinematic viscosity of fluid and turbulent viscosity, respectively. \mathbf{F} is the source term that accounts for the momentum transfer between the two phases.

The turbulence model used for solving the RANS equations in this study is the standard k- ϵ model, which is one of the most commonly used turbulence models in computational fluid dynamics. The standard k- ϵ model is efficiently combined with the Lagrangian particle tracking methods because turbulent variables instantly estimate the scale of the velocity perturbations caused by turbulent eddies, and the average lifetime of eddies. In the standard k- ϵ model, two additional transport equations and two dependent variables are introduced: the turbulent kinetic energy (k), and the turbulent dissipation rate (ϵ). Consequently, the turbulent viscosity (μ_T) is modeled as

$$\mu_T = \rho C_\mu \frac{k^2}{\epsilon}, \quad (3.2)$$

where C_μ is a model constant as listed in **Error! Reference source not found..**

The transport equation for the turbulent kinetic energy is

$$\rho(\mathbf{u} \cdot \nabla)k = \nabla \cdot \left[\left(\mu + \frac{\mu_T}{\sigma_k} \right) \nabla k \right] + P_k - \rho \epsilon, \quad (3.3)$$

where the term P_k is the production term that is define as

$$P_k = \mu_T [\nabla u : (\nabla u + (\nabla u)^T)]. \quad (3.4)$$

The transport equation for the turbulent dissipation term is

$$\rho(u \cdot \nabla) \varepsilon = \nabla \cdot \left[\left(\mu + \frac{\mu_T}{\sigma_\varepsilon} \right) \nabla \varepsilon \right] + C_{\varepsilon 1} \frac{\varepsilon}{k} P_k - C_{\varepsilon 2} \rho \frac{\varepsilon^2}{k}. \quad (3.5)$$

The default values of the dimensionless constants in these equations are listed in Table 2 and determined from experimental data by (Wilcox, 1993)

Table 2. Model constants

Constant	Value
C_μ	0.09
$C_{\varepsilon 1}$	1.44
$C_{\varepsilon 2}$	1.92
σ_k	1.0
σ_ε	1.3

3.1.2. Solid-phase modeling

The particle tracing module in COMSOL Multiphysics® was used for modeling particle trajectories in particle-laden pipe flow and computing the particle-wall interactions.

All particles are assumed rigid and spherical, and they are randomly released at the inlet. Particle velocities have the same value as the fluid velocity at the particle positions. The particle equation of motion is a mathematical model that describes particle movement in a particle-laden flow. It essentially relies on the application of Newton's second law to the particle:

$$m_p \frac{dv}{dt} = F_m + F_{f \rightarrow p} + F_{p \rightarrow p} \quad (3.6)$$

Based on Newton's second law, the product of particle mass (m_p) times particle acceleration (dv/dt) is equal to the forces exerted on particles. These forces are categorized into three main groups; mass forces (F_m), forces exerted by the fluid on the particle ($F_{f \rightarrow p}$), and forces exerted from the particles on the current particle ($F_{p \rightarrow p}$). In this study, the particle-particle interactions are neglected as the system is in the dilute phase. The total force acting on particles in a fluid flow includes many physical phenomena, involving drag force, gravity force, buoyancy force, added mass effect, lift force, pressure gradient force, and Brownian force. The buoyancy force is due to the hydrostatic pressure over the particle surface and can safely be neglected as the particle density is several orders of magnitude greater than the air density. In this study, the drag force and gravity are assumed to be the dominant factors in determining the particle trajectories. Other types of forces such as the history force, the shear lift force, and the rotational lift are insignificant and therefore neglected.

Thus, the equation of motion for the particles can be reduced to the following equation proposed by Crowe & Michaelides (*Multiphase Flow Handbook*, 2016) for a particle that is influenced only by the drag and gravitational force:

$$m_p \frac{dv}{dt} = F_D + F_g. \quad (3.7)$$

In most engineering applications involving gas-solids flows, the only relevant mass force is the gravitational force that causes the particle to move along gravity. Among the different forces exerted on a particle by the surrounding fluid, the drag force plays the dominant role in most particle-laden flows. The aerodynamic drag force acting on a particle is defined as (Crowe *et al.*, 2011),

$$F_D = \frac{1}{\tau_p} m_p (u - v), \quad (3.8)$$

where m_p is the particle mass (kg), \mathbf{u} is the fluid velocity at the particle's position (m/s), \mathbf{v} is the particle velocity, and τ_p is the particle relaxation time (s), which is defined as

$$\tau_p = \frac{4}{3} \frac{\rho_p d_p}{\rho C_D |u - v|}. \quad (3.9)$$

In the above equation, ρ_p is the particle density (kg/m³), d_p is the particle diameter, and C_D is the dimensionless drag coefficient. The drag coefficient is mainly a function of the particle Reynolds number, which determines the appropriate drag law. The relative Reynolds number for a spherical particle is calculated as

$$Re_p = \frac{\rho |u - v| d_p}{\mu} \quad (3.10)$$

in which μ is air dynamic viscosity, \mathbf{u} is the fluid velocity at particle position, \mathbf{v} particle velocity, and d_p is the particle diameter.

The Schiller-Naumann model was used for describing the drag coefficient. This model is suitable for dilute flows with rigid spherical particles (Schiller and Naumann, 1935). The drag coefficient in this model is defined as

$$c_d = \begin{cases} \frac{24}{Re_p} (1 + 0.15Re_p^{0.687}) & Re_p < 1000 \\ 0.44 & Re_p > 1000 \end{cases} \quad (3.11)$$

In most engineering cases, the Reynolds-Averaged Navier-Stokes (RANS) approach is used where the turbulent eddies are solved by estimating their kinetic energy and dissipation rate (Patel, Rodi and Scheuerer, 1985; Chen and Kim, 1987; Kalitzin *et al.*, 2005). In this approach, the fluid velocity at the particle's position (\mathbf{u}') is not given deterministically. Instead, it is treated as a linear combination of the mean velocity (\mathbf{u}) and a turbulent perturbation term ($\Delta\mathbf{u}$). Therefore, the drag force formulation is modified as follows

$$F_D = \frac{1}{\tau_p} m_p (\mathbf{u}' - \mathbf{v}), \quad (3.12)$$

$$\mathbf{u}' = \mathbf{u} + \Delta\mathbf{u}$$

The kinetic energy and dissipation terms derived by solving the k- ϵ turbulent model determine the amplitude and direction of the velocity perturbations ($\Delta\mathbf{u}$).

3.1.3. Phase coupling

In order to determine the most proper approach to simulate a particle-laden flow, it is crucial to identify the type of coupling between the two phases, which is different in dilute and dense flows. In dilute flows, the particles move as individual entities, and their motion is dominated by the effect of the fluid, whereas in the dense phase, the particle motion is dominated by the interactions between the particles (Crowe *et al.*, 2011). Dilute flows are often characterized by low particle volume fraction ($\varphi < 5\%$), whereas particle-laden flows with concentrations higher than 5% are considered dense flows (Patankar and Joseph, 2001).

Four different coupling regimes are defined for gas-solids flows. In the one-way coupling regime, the particles have a negligible effect on the flow of the carrier phase, and only flow affects the particle motion. Conversely, in the two-way coupling regime, the fluid flow field is affected by the presence of the particles. In the four-way coupling regime, the particle-particle interactions play a vital role in the flow dynamics and should therefore be considered (Strömberg *et al.*, 2011).

There is no parameter that clearly establishes a threshold between dilute and dense flows. According to the well-known Elghobashi's map, particle volume fraction threshold values define the boundaries between the different flow regimes. One-way coupling occurs for solid volume fraction lower than 10^{-6} , and two-way coupling occurs for solid volume fraction between 10^{-6} and 10^{-3} . Four-way coupling is associated with a solid volume fraction above 10^{-3} (Elghobashi, 1991). Investigation of the particle-wall interactions in a dilute particle-laden flows is of interest in this study. Therefore, solid and gas phases are coupled in a one-way manner.

3.1.4. Geometry and mesh

Numerical simulations are conducted in a three-dimensional cylindrical coordinate. The pipe is assumed horizontal on the x-axis with the inlet on the left and the outlet on the right side. The spanwise and wall-normal directions of the particle-laden flow

is depicted by the y-axis and z-axis, respectively. The length of the cylinder is 1 m and the diameter is 4.76 mm.

To ensure the accuracy of the CFD model and to reduce the computational time, a grid independence test was performed. In this study, particle-wall mean collision number was considered as the quantities of interest. The grid independence test was initiated from an extra coarse mesh with a low number of elements, and the accuracy of results was examined as the mesh elements were increased. The refinement of the mesh was done to find a fine enough mesh where the quantities of interest show minimum changes for any further mesh refinement. More precisely, the mesh refinement was done until the variation of the results between two successive mesh densities were less than 5%, confirming that the result is grid-independent, and further discretization has no substantial impact on the simulation results.

The grid independence test was performed for a three-dimensional pipe with 0.00476 m diameter and 1 m length. Particle-wall collision numbers were calculated for 10-micron particles. The descriptions of four different grids, including Fine, Normal, Coarse, and Extra coarse, with a different number of elements are summarized in Table 3.

Table 3. Specifications of used grids.

Mesh	Number of elements	Minimum element quality	Average element quality	Element volume ratio
Fine	2383517	0.1001	0.7405	0.006482
Normal	1330473	0.1034	0.7385	0.008314
Coarse	531686	0.1188	0.7135	0.01168

Extra coarse	119042	0.1472	0.7235	0.03315
--------------	--------	--------	--------	---------

For the four types of mesh, the particle-wall mean collision numbers were computed, and numerical results were compared with experimental results proposed by (Matsusaka *et al.*, 2002). It is evident from Figure 8 that the numerical results obtained using Normal mesh with 1330473 elements are independent of the grid size and are in good agreement with experimental results. Increasing the number of elements to 2383517 in Fine mesh expanded the computation time, whereas the calculated results did not show significant improvement. Therefore, Normal mesh was picked as the optimal mesh for our simulations.

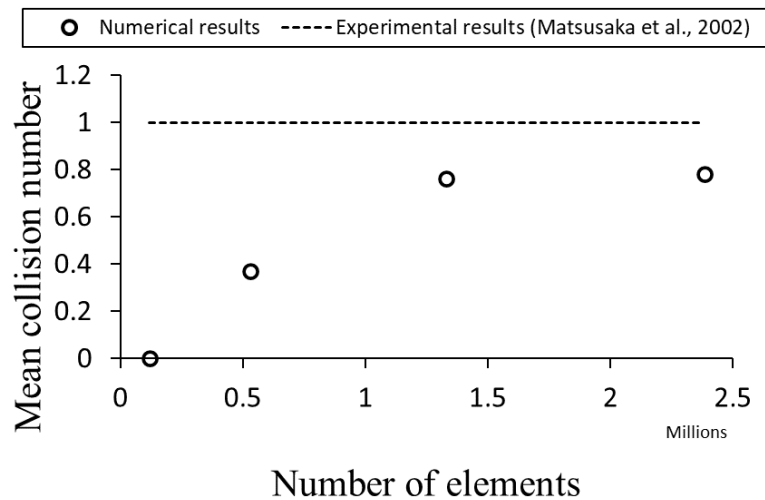


Figure 8. Comparing calculated particle-wall mean collision numbers using different mesh sizes with experimental results.

3.1.5. Computation of particle-wall interactions

The Auxiliary Dependent Variables (ADV) feature in COMSOL is used to keep track of variables like particle residence time, particle trajectory length, and particle collisions with surrounding boundaries. A dependent variable was defined on particles, and an

additional ordinary differential equation was solved for each particle. Therefore, it is possible to calculate the times that each particle collides with the pipe wall.

In this thesis, first, an ADV feature was added to the time-dependent particle tracking study. Then, the term 'Collisions' was defined as the dependent variable name and selected to calculate the integrated variable over time. It is possible to change the value of the ADV whenever a particle interacts with a boundary. For this purpose, an expression (Collisions+1) is entered for the new value of the dependent variable. This means that every time particles collide with the boundaries, this expression updates the value of the dependent variable.

3.2. Prediction of particle-wall collision number using Artificial Neural Networks

This chapter presents a methodology for machine-learning-based prediction of particle-wall collision numbers in particle-laden pipe flows. The developed model uses an input data set on various physical parameters of particles and flow systems achieved through computational fluid dynamics (CFD) in the previous chapter to predict the number of collisions. An artificial neural network with six inputs, namely, particle size, particle density, air velocity, the vertical velocity of particles, pipe diameter, and pipe length, was designed and trained to predict particle-wall mean collision numbers.

Developing a neural network is a four-step process including database generation and preparation, designing network architecture, network training, and network testing.

3.2.1. Database generation

The first step for developing a neural network model is to generate a database. In this study, the particle-wall mean collision numbers calculated via CFD simulations are the targets that are collected for various input parameter combinations, including particle size, particle density, vertical particle velocity, air velocity, pipe length, and

pipe diameter. A brief summary of the database generated for developing a neural network, along with the inputs and output range, is presented in Table 4.

Table 4. Network inputs and output.

Parameter	Range
<i>Network inputs</i>	
Particle size (micron)	10-600
Particle density (kg/m ³)	1410-7850
Pipe diameter (m)	0.002-0.006
Pipe length (m)	0.25-1.5
Average air velocity (m/s)	6.5-36
Particle vertical velocity (m/s)	0-1.2
<i>Network output</i>	
Particle-wall mean collision number	0.6-80

3.2.2. Data preprocessing

In this study, the values of the input variables are highly scattered by several orders of magnitude, which makes it challenging to explore the influence of each parameter on particle-wall mean collision numbers, labeled as the model output. Therefore, data normalization is a vital step in preparing data for artificial neural networks. For this purpose, Min-Max normalization (equation) was used, and all data points were normalized between 0 and 1. In this method, the minimum value of each variable is transformed into 0, and the maximum values are transformed into 1. Every other value between the minimum and maximum values is converted into a decimal between 0 and 1.

$$x'_i = \frac{x_i - x_{min}}{x_{max} - x_{min}}, \quad (3.13)$$

where x'_i is the i^{th} normalized data, and x_{min} and x_{max} are the minimum and maximum value of data points, respectively.

3.2.3. Network topology

A three-layer neural network was used to train the prepared database. Figure 9 shows a schematic of the network topology. The first layer of the network is the input layer which contains six neurons equal to the number of input parameters. The second layer is the hidden layer, and the number of neurons in this layer is one of the model's hyperparameters which needs to be accurately tuned to get a reliable network. The detailed information on determining the number of neurons in the hidden layer will be presented in chapter 4. The network's last layer is the output layer with one neuron corresponding to the particle-wall mean collision number.

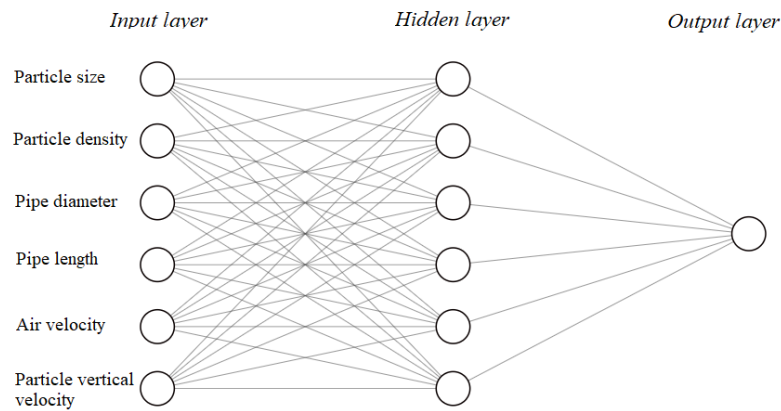


Figure 9. Network topology .

3.2.4. Network training

In the training phase of the neural network development, an optimal set of weights and bias values are computed for the whole network. The prepared database was

randomly split into the training, validation, and testing sets for training a neural network. 70% of the database, including 137 data points, was assigned for the training set. 15% of the database (30 data points) was employed for the validation of the network, and the remaining 15%, including 30 data points, was employed for testing the network performance and is called test data. The network was not trained with the data in the test set.

Different algorithms are available for training neural networks. In this study, the Levenberg-Marquardt algorithm (Srinivasan and Saghir, 2013, 2014a, 2014b) was employed for training the network for its robustness and fast convergence. This algorithm typically requires more memory but less time. This algorithm minimizes a mean square error function over a multi-dimensional parameter space, and the training process automatically stops if generalization stops improving. In the Levenberg-Marquardt algorithm, first, the network's response for the training set is evaluated using initial random weights and biases produced by Nguyen and Widrow's initialization algorithm. In the next step, the values of the weights and biases of the neural network are updated based on the error between the desired response and the response predicted by the network. This process persists until the error is diminished to a preferred level.

3.2.5. Network testing

After the training process, the network's performance was evaluated using the test set, which contains 15 % of the database, and the model has not trained on them. Root Mean Square Error (RMSE) was used for measuring the network's performance. Due to the different values of initial weights and biases that each network uses during the training process, the performance of generated networks is not identical. Hence, to obtain a realistic network performance, 30 neural networks with different initial weights and biases were generated using a similar training set, and the average value of RMSEs calculated for all the 30 networks was considered the network performance.

The results regarding network testing are presented in section 4.7.2 of the Results and Discussion chapter.

3.3. Modeling particle tribocharging

This section presents the mathematical model of particle tribocharging in particle-laden flows, along with the experimental powder tribocharging and charge measurement procedure. The initial charge on the surface of particles released into the pipe flow is assumed to be negligible. The volume fraction of particles was considered very low compared to the volume fraction of the fluid phase to satisfy the dilute condition. In dilute particle-laden flows, particle-particle interactions are negligible, and particle-wall collisions are the leading cause of tribocharging. Particles and pipes are assumed to be different in material, and when a collision happens, electrostatic charge transfer occurs due to differences in work functions.

3.3.1. Experimental charge measurement

For validating the numerical simulation results of tribocharging, the experimental data was obtained from a research team at Howard University.

The experimental setup consists of three sections, including a sample feeder, a tribocharging tube, and a Faraday cup connected to an electrometer, as illustrated in Figure 10. The sample feeder is a 50 ml container that is connected to a high-pressurized air supply, and the airflow rate is adjusted using a flowmeter before introducing dry air at the bottom of the sample feeder. The tribocharging unit is a PTFE tube with 150 cm length and 4.76 mm inside diameter. At the inlet, the tribocharger tube is connected to the sample feeder and at the outlet to a Faraday cup (Monroe Electronics Inc., Lyndonville, NY, USA) that is connected to an electrometer (Model 6514, Keithley Company, Cleveland, OH, USA) for charge measurements.

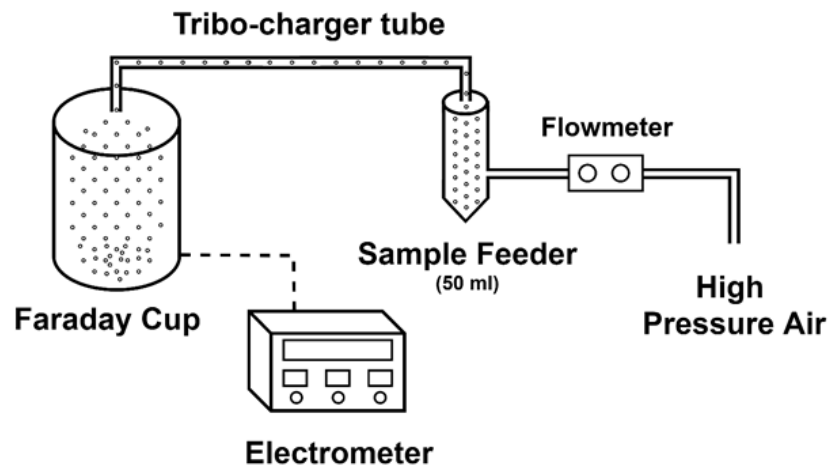


Figure 10. Experimental set up for powder tribocharging and charge measurements (Howard university).

Samples are organic flours (yellow pea) that are sieved with different sieve numbers, and the range of particle size prepared for charge analysis is between 25 and 380 microns. (The protein content of each particle size group was determined using a chemical protein digestion method to investigate the influence of powder chemical composition on the charging behavior of particles). Twenty grams of samples were initially placed inside the sample feeder, and dry air was introduced at the bottom of the sample feeder at the adjusted airflow rate of 7 LPM. Particles were fluidized in the feeder, and only a few of them enter the charging tube at a time, which satisfies the dilute condition. During transfer in the charging tube, particles repeatedly collide with the wall, and charge transfer occurs due to different work functions of contact surfaces. Charged particles are directly dispensed into the Faraday cup, where an electrometer measures the potential difference that occurred between the inner wall and the outer wall of the Faraday cup. The mass of the particles accumulated in the Faraday cup was measured with an analytical balance, and the measurements were reported as charge per mass ratio of the samples. All charge measurements were performed with ten replicates at room temperatures for each particle size group, and

the entire apparatus was flushed with dry air between each measurement to avoid any inaccuracy through tribocharging analysis.

3.3.2. Tribocharge modeling

Two different types of contacts may occur during particle transport in particle-laden flows: particle-particle interaction and particle-wall interaction (Crowe *et al.*, 2011). In the dilute phase, inter-particle collisions are negligible; consequently, the amount of charge transfer via particle-particle collisions is insignificant. Therefore, the primary mechanism of charge transfer in dilute particle-laden flows is particle-wall interactions. The calculation of transferred charge between particles and the wall could be described based on the condenser model, which considers particle and wall surfaces as the two plates of a capacitor where charge transfer occurs due to different work functions of two materials in contact (Masuda, Komatsu and Inoya, 1976; Itakura *et al.*, 1996; Masuda *et al.*, 1998; Matsusaka, Ghadiri and Masuda, 2000; Tanoue *et al.*, 2001; Ema *et al.*, 2003; S. Matsusaka *et al.*, 2010).

In particle-laden pipe flows, particles repeatedly collide with the inner wall, due to which tribo-charging takes place. Based on the condenser model, it is possible to formulate the particle charge generated by repeated impacts in gas-solids pipe flow. In this study, a tribocharging model is used based on repeated particle impacts on the wall, as proposed by (Matsusaka and Masuda, 2003). According to this model, when a particle moves from point x to point $x+\Delta x$ along the pipe axis, the variation of charge per mass ratio of particles as a function of the number of particle-wall collisions (n) is derived from the exponential equation 3.14:

$$\begin{aligned} \frac{\Delta q}{m_p} &= q_m(x + \Delta x) - q_m(x) \\ &= (q_{m\infty} - q_{m0}) \left\{ \exp\left(-\frac{n(\Delta x)}{n_0}\right) \right\} \left\{ 1 - \exp\left(-\frac{n(\Delta x)}{n_0}\right) \right\}, \end{aligned} \tag{3.14}$$

where q_{m0} and $q_{m\infty}$ are the particle charge per mass ratios at $x = 0$ and $x = \infty$, respectively, and n_0 is the dimensionless characteristic number of particle electrification given by (Masuda, Komatsu and Iinoya, 1976)

$$n_0 = \frac{\pi D_p^2}{2kS(1+\alpha)}, \quad (3.15)$$

and the particle charge per mass ratio at $x = \infty$ is given by

$$q_{m\infty} = \frac{3\varepsilon_0 V_c}{\rho_p D_p z_0 (1+\alpha)}, \quad (3.16)$$

where D_p is particle diameter, k is dimensionless charging efficiency, S is the contact area, ε_0 is the absolute permittivity of gas ($8.854 \cdot 10^{-12}$ F m⁻¹), V_c is the contact potential difference between the surfaces, z_0 is the critical gap between the particle and the wall. This is the cut-off distance for charge transfer and, according to literature, considered to be 10^{-9} m (Grosshans and Papalexandris, 2017).

α is the ratio of space charge effect to image charge effect derived as

$$\alpha = \frac{3}{4} m \frac{\rho_g D_i \bar{u}}{\rho_p D_p \bar{v}}, \quad (3.17)$$

where m is the mass flow ratio of particles to gas (dimensionless), ρ_g is gas density, ρ_p is particle density, D_i is the inner diameter of the pipe, D_p is particle diameter, \bar{u} and \bar{v} are average velocities of gas and particle, respectively.

For dilute phase flow where $\alpha \ll 1$, Eq. (Error! Reference source not found.) is revised as

$$\frac{\Delta q}{m_p} = -aq_{m0} - b, \quad (3.18)$$

where

$$a = \frac{2n(\Delta x)kS}{\pi D_p^2}, \quad (3.19)$$

and

$$b = -\frac{6\varepsilon_0 V_c n(\Delta x)kS}{\pi D_p^3 \rho_p z_0}. \quad (3.20)$$

Assuming that the initial charge per mass of particles is negligible ($q_{m0} \approx 0$), the total transferred charge per mass is calculated by

$$\frac{\Delta q}{m_p} = \frac{6\varepsilon_0 V_c n(\Delta x)kS}{\pi D_p^3 \rho_p z_0}. \quad (3.21)$$

It must be noted that the value of transferred charge per mass depends on both physical properties and the material of contacting surfaces. Collision number, pipe length, and particle size are physical properties that influence the tribocharging of

particles. On the other hand, contact potential difference and charging efficiency are essential factors that are determined by the chemical composition and morphology of the contacting surfaces.

The contact potential difference (V_c) between contact surfaces depends on their work functions which is determined by the material composition. Therefore, calculating contact potential difference requires the values of work functions for both the particle and the wall, which are not available in this study. Another way of calculating the contact potential difference between contact bodies is Kelvin-Zisman method, an experimental procedure that determines the contact potential difference of materials compared with Au or Pt as reference materials (Masuda *et al.*, 1995). Since this method was not accessible to this study, the contact potential differences was calculated as a fitting parameter.

Triboelectrification is a surface phenomenon, and the amount of charge transfer during the contact process significantly depends on the properties of the contact surfaces, such as surface roughness and surface material which determines the mechanical properties of the surfaces. For instance, Young's modulus and Poisson's ratio of contact surfaces determine the elasticity of contact bodies, and the total contact area engaged in the tribocharging process is estimated considering the deformation of contact bodies. According to the Hertzian theory of contact, the contact surface's relative velocity and the contact area's elasticity influence the contact area (Johnson, 1989).

Assuming that particles are spherical and elastic with a smooth surface, the maximum contact area during impact with a wall can be calculated based on the equation proposed by (Matusaka and Masuda, 2003),

$$S = 1.36k_e^{2/5} \rho_p^{2/5} D_p^2 v_i^{4/5}, \quad (3.22)$$

where k_e is the elasticity parameter, ρ_p is the particle density, D_p is the particle diameter, and v_i is the impact velocity of the particle. The elasticity parameter is calculated based on the following equation,

$$k_e = \frac{1 - \nu_1^2}{E_1} + \frac{1 - \nu_2^2}{E_2} \quad (3.23)$$

where E is the Young's modulus, ν is the Poisson's ratio, and subscripts 1 and 2 indicate the particle and the wall, respectively. Table 5 shows Young's modulus and Poisson's ratio for the wall material (PTFE) and particles used in this study according to (Molenda *et al.*, 2006).

Table 5. Particle and wall mechanical properties.

Material	Young's modulus (GPa)	Poisson's ratio
PTFE (wall)	0.390-0.750	0.460
Wheat flour (particles)	17.1-18.5	0.22-0.26

In summary, in this section, a dilute particle-laden flow is considered wherein spherical particles with zero initial charge enter the pipe and become electrically charged due to the collision with the pipe wall. The total amount of charge generated depends on various physics-based and material-based variables. The number of particle-wall collisions is a physics-based parameter that will be calculated via CFD simulations. Material-based parameters such as contact potential difference between particle and pipe wall and charging efficiency will be estimated as fitting parameters

using the particle-wall collision numbers achieved via CFD and experimental charge measurement data.

In the ensuing chapter, results regarding particle-wall collision numbers obtained through CFD are presented, and the performance of the neural network proposed for predicting mean collision numbers based on different properties of the solid and the gas phase is presented. Finally, a tribocharging model based on the particle-wall mean collision numbers is developed and validated with experimental results.

Chapter 4. Results and discussion

In this chapter, the results of the numerical simulations for the fluid phase and particle tracking of the solid phase are presented followed by the results regarding the validation of the proposed neural network for predicting the particle-wall collision numbers. Subsequently, the results of particle tribocharging based on particle-wall interactions are discussed and compared with the results obtained through experimental charge measurements. A considerable number of physical parameters affect the particle-wall interactions in two-phase pipe flows. Therefore, this study focuses on the influence of particle size and density, particle Stokes number, the velocity of fluid and particles, pipe diameter and length on particle-wall collision numbers. The influence of particle-wall interactions on the tribocharging of particles are discussed at the end of this chapter.

A dilute turbulent particle-laden flow was considered in the simulation. The gas-phase flow was assumed to be incompressible and was described with Reynolds Averaged Navier-Stokes equations in an Eulerian framework. The particulate phase was assumed spherical particles with the same material and density. Each particle was treated as a point mass whose trajectory was calculated in a Lagrangian framework. The volume fraction of the solid phase was low compared to the volume fraction of the gas phase to satisfy the dilute condition. As a result, the particle-particle interactions and the influence of particles on the gas phase were neglected, and therefore, one-way coupling was used for coupling the solid and gas phases.

4.1. Continuous phase modeling

Figure 11a shows the velocity field implemented by the Eulerian solver for the fluid phase with $Re = 2700$ (average air velocity = 8.4 m/s). As the pipe has an extremely high aspect ratio, the coordinate axes are scaled independently to better visualize the geometry. It is clear that the magnitude of fluid velocity decreases in near-wall regions.

Figure 11b shows the turbulence time scale, which is the ratio of turbulent kinetic energy (k) to turbulent dissipation rate (ϵ) in the modeling domain. According to this graph, the turbulent time scale is more significant at the center of flow (red zone), and it decreases near the wall (blue zone), implying that eddy lifetimes are much shorter near walls. Before proceeding with the particle tracing simulation, it is beneficial to plot the turbulence time scale as it shows the minimum resolution in the time needed to capture the particle-eddy interactions accurately. In this study, the minimum turbulent time scale near the wall is 1×10^{-3} s, and the time step selected for the time dependent particle tracing simulation was 1×10^{-5} which guarantees to capture all particle-eddy interactions.

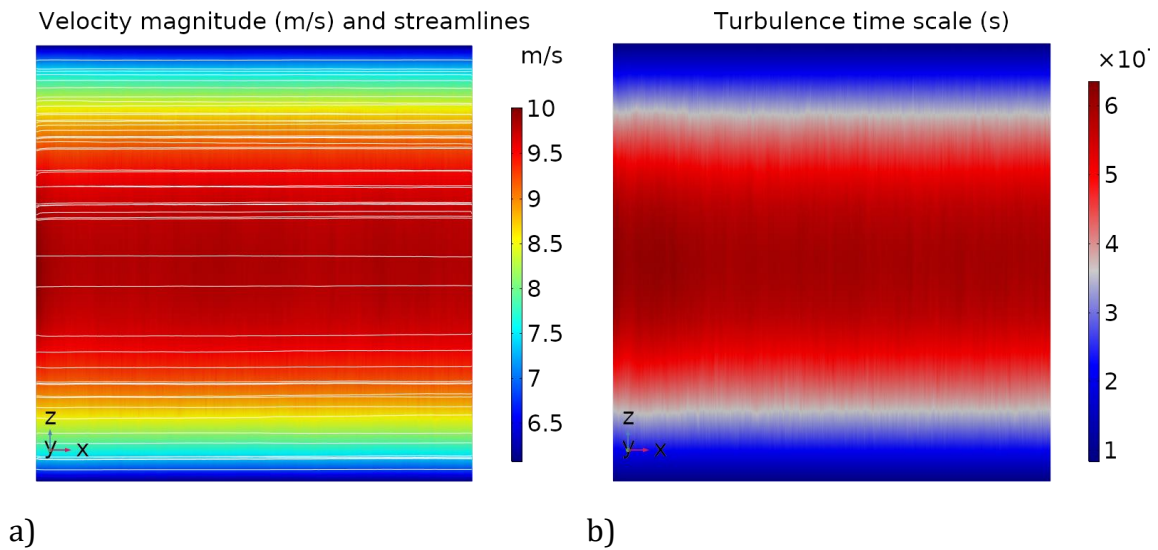


Figure 11. The velocity magnitude and streamlines of turbulent flow with $Re=2700$ (a) and turbulence time scale profile (b).

4.2. Number of released particles into the system

It is crucial to determine how many particles will need to be released through simulations to investigate the influence of various parameters on the particle-wall interactions. Therefore, the first set of analyses examined the impact of released

particles number on the mean particle-wall collision numbers. Particles are randomly released into the pipe flow with different initial positions, determining the particle's trajectory during transport. The particle's initial position affects the particle velocity, which consequently affects particle-wall collision numbers. The term Mean Collision Number has been used to depict a realistic number of collisions per particle. For calculating the mean collision number of particles, the number of released particles should be determined to get a reasonable average of collision numbers and reduce the computation time as much as possible.

For this purpose, several simulations were performed with different numbers of released particles, and the mean collision number and the computation time for each case were compared. All simulations were performed by releasing 100-micron particles into a pipe with 0.00476 m diameter and 1 m length, and the air velocity was 8.4 m/s. Table 6 provides the results obtained from the simulations with various numbers of released particles. Every recorded mean collision number is the average of four simulation runs. It was evident that particle-wall collision number calculated by releasing only one particle into the system is unreliable because it only represents a particular particle released from a specific position. Therefore, the calculated collision number is reliable only when a particle is released from a similar position. It can be seen from the data in Table 6 that the computation time increases as the number of released particles increases. Figure 12 demonstrates that the mean collision number decreases as the number of released particles increases. Since particles are randomly released into the pipe flow, it is expected to record a slightly different mean collision number for each simulation. As a result, four simulations were performed for each condition, and the means and the standard deviations were reported in Table 1. Based on the data presented in Table 1, only four mean collision is recorded by releasing one single particle into the system and the computation time is minimum, as it was expected. Increasing the number of released particles to 10 particles results in a dramatic increase of mean collision number to 7.6 collisions per particle. When releasing 100 particles into the system, the mean collision number

does not significantly change compared to 10 released particles, and it takes almost 6 minutes for computation. While a further increase in the number of released particles substantially increases the computation time, no significant difference is observed for the calculated mean collision numbers. Therefore, releasing 100 particles would be a viable choice with a reasonable computation time. As a result, the release of 100 particles was considered as the base number for all other simulations to investigate the influence of various parameters on particle-wall mean collision numbers.

Table 6. The particle-wall mean collision numbers and computation times calculated for different numbers of released particles into the system.

Number of released particles	Mean collision number	Computation time	STDEV
1	4	1 min 13 s	0
10	7.6	2 min 11 s	0.2
100	7.3	6 min 15s	0.3
500	6.97	19 min	0.1
1000	6.92	31 m 2 s	0.1
2000	6.8	51 min 52 s	0.1
5000	6.7	108 min 23 s	0

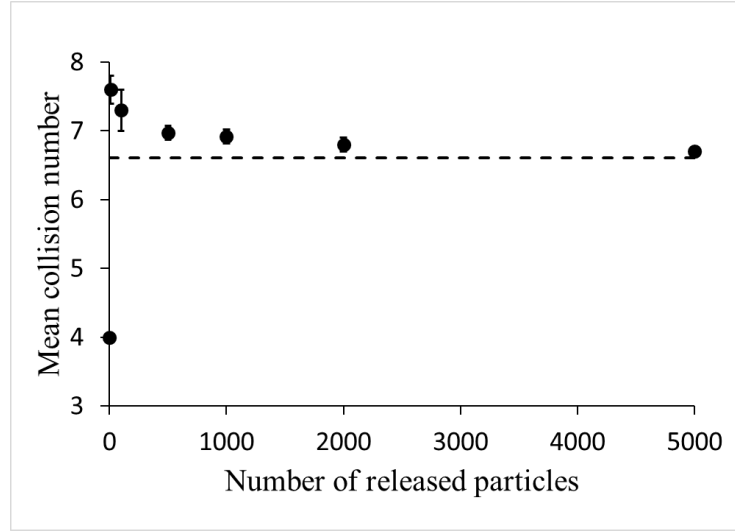


Figure 12. Calculated mean collision numbers for different numbers of released particles. The error bars represent the standard deviation.

4.3. Influence of particle Stokes number on particle-wall interactions

The ratio between the particle response time (τ_p), and the characteristic time scale of the fluid flow (τ_L) is defined as the particle Stokes number (St).

$$St = \frac{\tau_p}{\tau_L} = \frac{\rho_p d_p^2}{18\mu} \bigg/ \frac{k}{\varepsilon} \quad (4.1)$$

The particle response time (particle relaxation time) is the time required by the particle to respond to eddies in the flow. The value of particle response time depends on the particle size (d_p), particle density (ρ_p), and fluid viscosity (μ). Assuming that the turbulent time scale is constant, particles with a larger diameter and higher density require a longer time to respond to the fluid structures than particles with lower density and smaller sizes. Chan et al. conducted a direct numerical simulation of two-phase turbulent pipe flow for investigating the mechanism of particle transport within a range of Stokes number (Chan *et al.*, 2020). They observed three

regimes based on particle Stokes number, and our results are in good agreement with the results proposed in this study. Particles are categorized into three different groups based on the Stokes numbers, namely, low Stokes ($St < 1$), moderate Stokes ($1 < St < 10$), and high Stokes particles ($St > 10$).

At a very low Stokes number ($St < 1$), particles act like tracers that follow the fluid streamlines, but they do not have enough inertia to cross the eddies. The turbulent structures govern the transportation of these particles entirely. Therefore, they barely collide with the wall (Figure 13a). At intermediate Stokes numbers ($1 < St < 10$), particles have enough inertia to cross the eddies but not enough inertia to get back to the center streamlines. Therefore, they are trapped at low-velocity zones near the wall and repeatedly collide with the wall until they leave the pipe (Figure 13b). The transport mechanism of particles with intermediate Stokes numbers is affected by the turbulent structures and particle inertia. At very high Stokes number ($St > 10$), the effect of turbulent structures on particle transport is less pronounced than the intermediate Stokes values because these particles have very high inertia enables them easily cross the eddies and bounce back into the bulk medium after colliding with the wall (Figure 13c). Generally, the trajectory of particles with large Stokes numbers is unresponsive to the short time scales of the turbulent flow.

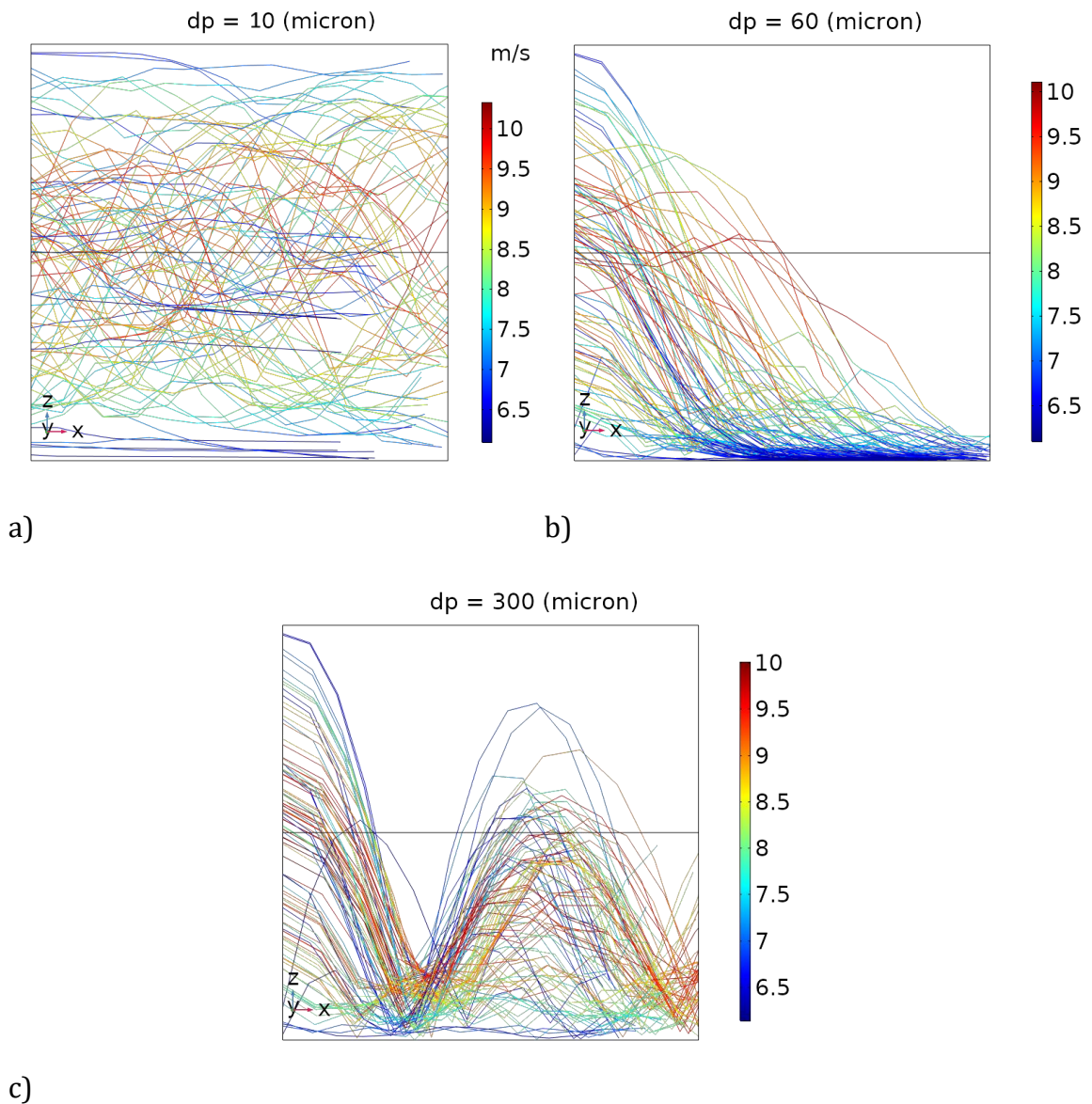


Figure 13. Particle trajectories for low (a), intermediate (b), and high (c) Stokes numbers. The color of trajectory lines shows the velocity magnitude (m/s) of particles. The x -axis points in the streamwise direction, the z -axis in the wall-normal direction, and the y -axis in the spanwise direction.

Figure 14 compares the number density of particles with different Stokes numbers near the pipe wall with the same flow conditions after one second period. The number density of particles describes the degree of concentration of particles in the domain. For an intermediate value of Stokes number (60-micron particles), the particles

cluster near the wall as they have enough inertia to cross the eddies and enter the near-wall region. At very low Stokes number (10-micron particles), particles often follow the fluid streamlines and do not have enough inertia to cross the eddies. Whereas, at high Stokes number (300-micron particles), particles have very high inertia, which causes them not to be affected by the turbulence and reflect off into the mainstream after hitting the wall. Therefore, particles with low and high Stokes numbers show almost similar particle number densities near the wall and have a lower value than those with intermediate Stokes numbers. This explains the high rate of particle-wall collision numbers recorded for particles in the intermediate Stokes regime.

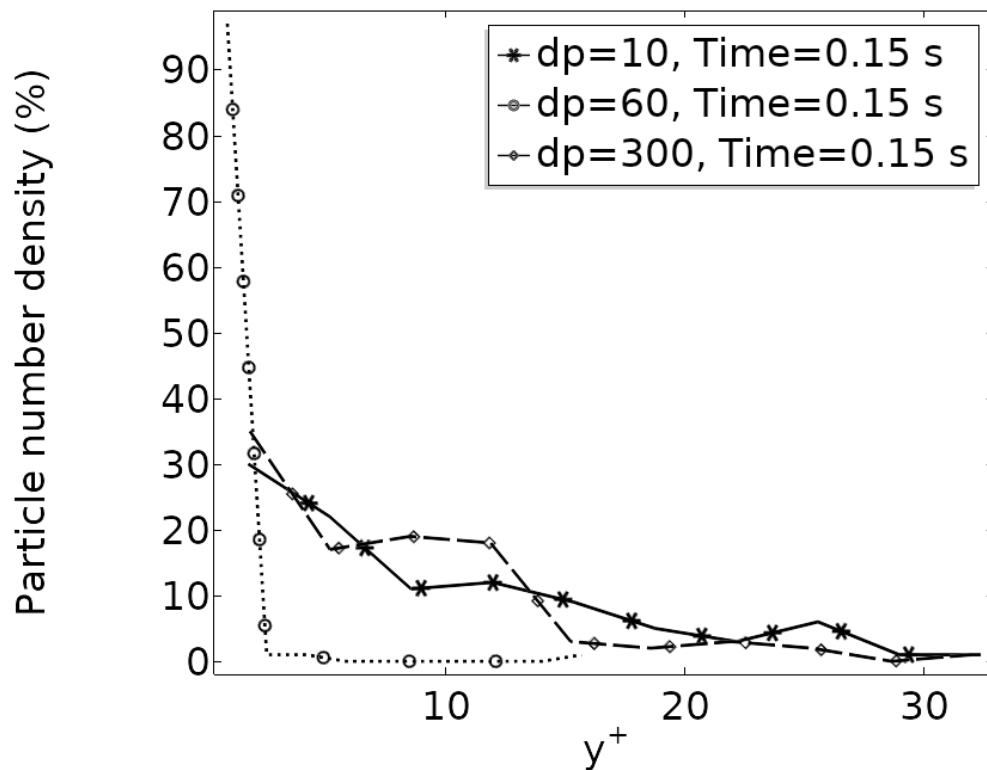


Figure 14. Comparison of near the wall particle number densities for different values of particle size (Stokes number).

For the case of low Stokes number ($St = 0.2$) the values of particle number density in the viscous layer at three different time steps ($t_1 = 0.02$, $t_2 = 0.05$, $t_3 = 0.15$) is depicted in Figure 15. This plot confirms that the particle number density in the region $0 < y^+ < 2$ is very low, reducing the chance of particle-wall collisions. The reason is that at low Stokes numbers, particles exactly follow the fluid streamlines. Therefore, particle trajectories are completely parallel to the wall, making it impossible to collide with the pipe wall. The particle number density graph shows peaks located between $y^+ = 2$ and $y^+ = 5$. An interesting finding shown by this graph is that the peak value grows over time and gradually gets closer to the wall, which is a sign of turbophoretic drift. Turbophoresis is defined as a two-phase process with different time scales. First, strong turbulent structures push particles towards the pipe walls and then, particles are slowly transported by weak turbulent structures. This phenomenon causes the particle concentration to increase near the wall region. Similar results were proposed by (Grosshans and Papalexandris, 2017).

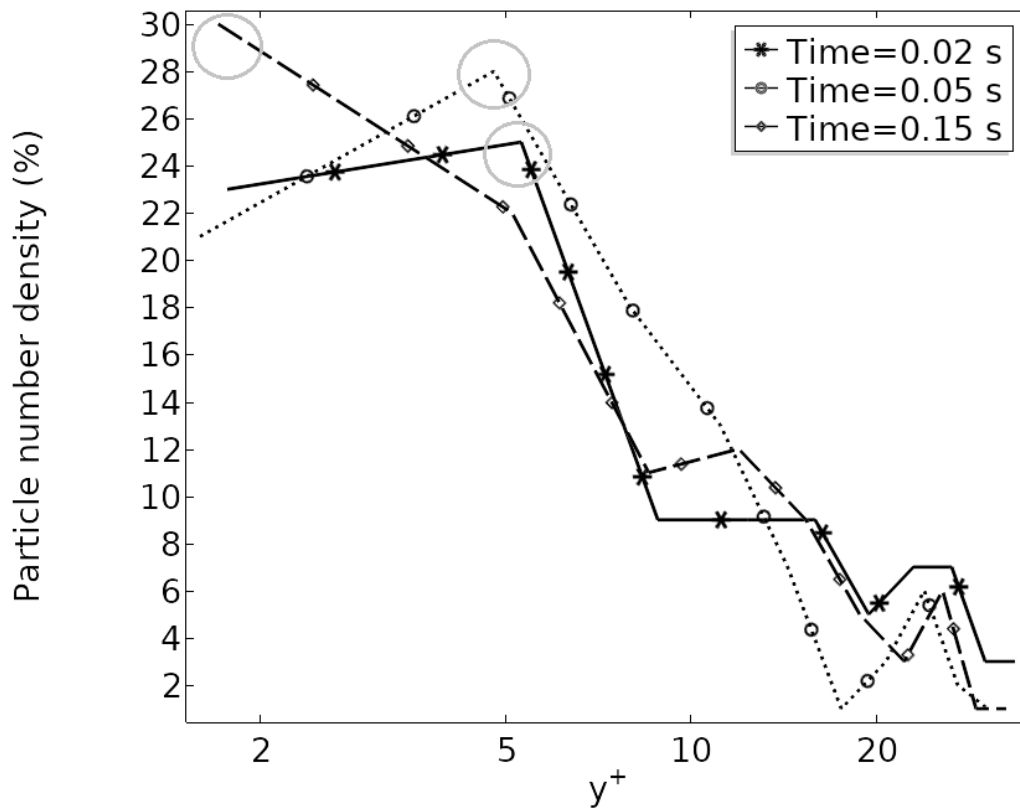


Figure 15. Evolution of particle number density in the near-wall region for low Stokes particles.

A similar graph was produced for the intermediate Stokes case ($St = 2$) while keeping all parameters constant. At intermediate Stokes numbers, particles no longer follow the exact fluid streamlines. They have enough inertia to cross the eddies and collide with the wall, but they can not return to the center streamlines. Therefore, they cluster near the wall. This phenomenon of particle agglomeration in the viscous sublayer is often known as turbophoresis, which is more pronounced for the intermediate Stokes regime (Grosshans and Papalexandris, 2017). For very low Stokes numbers the turbophoresis effect is less pronounced as particles act like tracers, and the fluid phase fully governs particle motion. Figure 16 shows the particle number density of moderate Stokes particles near the wall region. Similar to the low Stokes case explained, the maximum value of the particle number density increases

as time goes by. However, in this case the particle number density in the region $0 < y^+ < 2$ is very high, which enhances particle-wall interactions. Moreover, compared to the low Stokes case, the peak value of the particle density number is considerably moved towards the wall, and the majority of particles reached the region $y^+ < 2$ at time t_3 , consequently resulting in a substantial increase of particle-wall collisions.

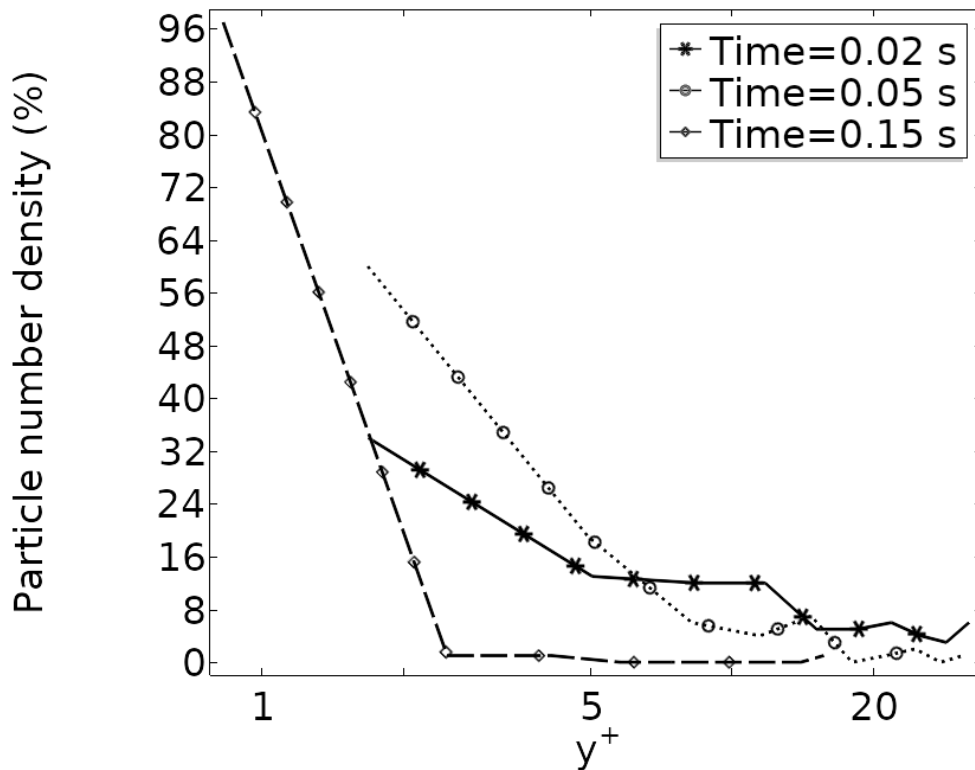


Figure 16. Evolution of particle number density in the near-wall region for intermediate Stokes particles.

The particle number density of high Stokes particles ($St = 36$) is depicted in Figure 17. At high Stokes numbers, particle trajectories are less affected by the turbulence structures and particle dynamics dominated by particles' inertia. Consequently, the calculated particle-wall collision numbers are almost constant in every simulation

run. This fact will enhance the constancy of particle tribocharging predictions based on particle-wall collision frequency for high Stokes particles.

Comparing the particle number density profile of high Stokes particles in Figure 17 with low and moderate Stokes numbers in Figure 15 and Figure 16 confirms that particle distribution is more uniform in the region close to the wall for the higher Stokes numbers. This implies that the turbophoretic drift is less pronounced for particles with a higher Stokes number, and particle agglomeration progresses more slowly compared to the cases with low and moderate Stokes numbers. This phenomenon could be explained by the term "local Stokes number" that was proposed by (Marchioli and Soldati, 2002). They explained that by increasing the response time of large particles and decreasing turbulent time scale, the local Stokes numbers of high inertia particles increase as they approach the wall. Therefore, the trajectories of these particles are not affected by turbulent structures near the wall as they have enough inertia to cross these structures and bounce back into distant layers without getting trapped in the viscous sublayer. The sudden rise of particle number density in different times which are notable in Figure 17 exhibit the particles reflections after colliding with the wall.

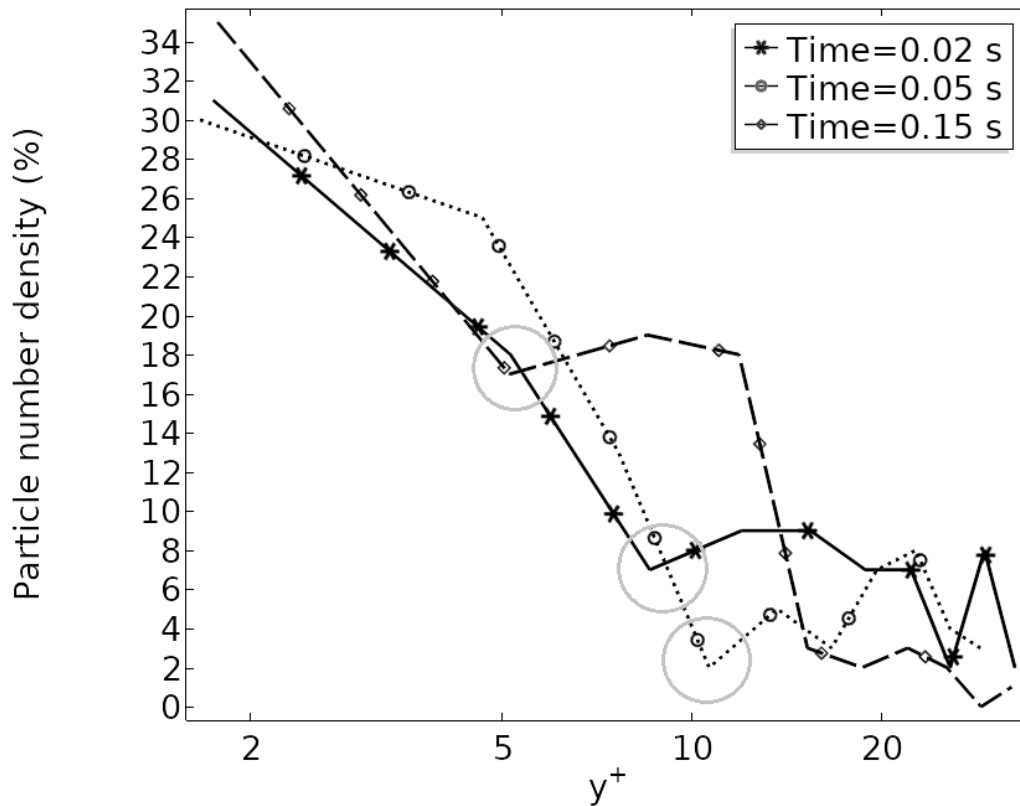


Figure 17. Evolution of particle number density in the near-wall region for high Stokes particles.

4.4. Influence of particle size and density on particle-wall interactions

To investigate particle size's influence on particle-wall interactions, particles with the same densities but different diameters ranging from 5 to 300 microns were released into a pipe with a 1-meter length and 0.00476-meter diameter. The air velocity in the pipe was 8.4 ms^{-1} , and 100 particles of each size were released into the system in every simulation.

Simulation results confirmed that small particles ($< 10 \text{ micron}$) have a very low Stokes number ($St < 1$), which causes them to act like tracers and completely follow the turbulent streamlines. Therefore, they show minimum interaction with the wall. Particles between 50 to 100 microns in size have intermediate Stokes number ($1 < St < 10$). The motion of these particles depends on both the turbulent effect and inertia

of particles. These particles have enough inertia to cross the turbulent eddies and collide with the wall, but they do not have enough inertia to reflect the center streamlines. Therefore, they repeatedly collide with the wall until they exit the pipe. Particles larger than 100 microns have a high Stokes number ($St > 10$), which means the particle response time is much higher than the turbulent time scale, and consequently, particles do not respond to the changes in the turbulent flow. Therefore, the motion of large particles is entirely governed by their inertia, not the turbulent effect (Figure 18).

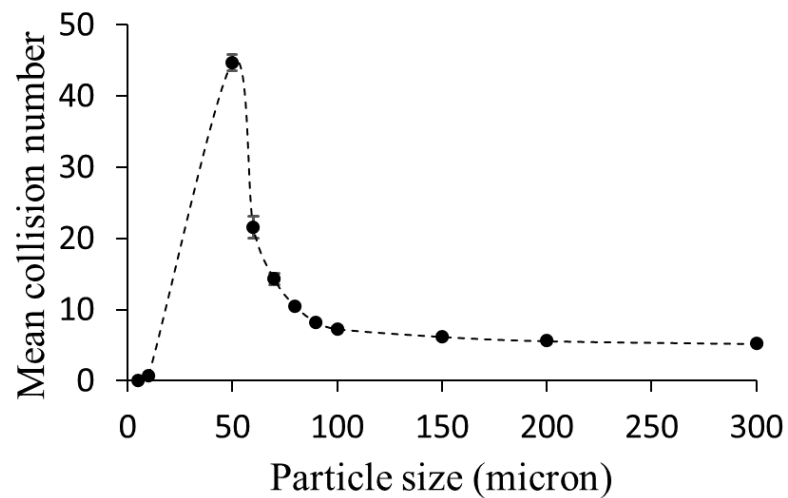


Figure 18. Influence of particle size on particle-wall mean collision numbers. Particles were released into a 1-meter pipe with 4.76 mm inner diameter and the air velocity was 8.4 (ms^{-1}).

Five different materials with different densities were selected to investigate the influence of particle density on particle-wall mean collision numbers. Table 7 shows the densities of particles used in simulations. In each density group, the mean collision numbers were calculated for 100-micron particles. Figure 19 shows that for different densities, the particle-wall collision number decreases by increasing the particle density. This could be explained by the relation of particle

density and particle response time (τ_p), as they are directly related. As particle density increases, they require much more time to respond to the changes in the turbulent flow, as is expected for particles with a high Stokes number. Therefore, they do not have enough time to follow turbulent streamlines, and their inertia mainly governs their motion.

Table 7. Density of materials used in simulations.

Material	Density (kg/m ³)
Flour	1440
PVC	1410
Glass beads	2420
Quartz sand	2650
Steel	7850

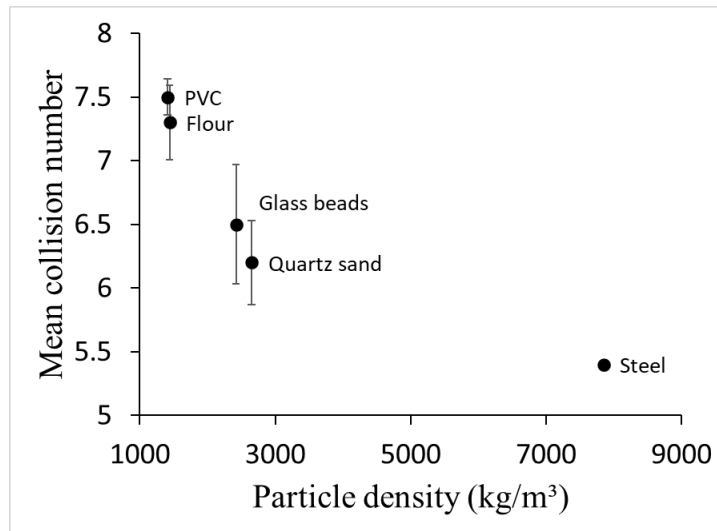


Figure 19. Comparing mean collision numbers of 100-micron particles with different densities. All particles assumed spherical particles released into a 1-meter pipe with 4.76 mm inner diameter and the air velocity was 8.4 ($m s^{-1}$).

4.5. Influence of pipe diameter and length on particle-wall interactions

Several simulations were performed using different pipe diameters and lengths with a similar average air velocity of 8.4 ms^{-1} to investigate the influence of pipe diameter and pipe length on the particle-wall mean collision numbers. Figure 20 shows that for inertial particles larger than 100 microns (high Stokes particles), the mean collision numbers decrease by pipe diameter since the distance between particles and the walls increases, and consequently, particles have to travel a longer distance to reach the wall. Different results were obtained for particles with intermediate Stokes number (60-micron). As it is demonstrated in Figure 20, for particles smaller than 100-micron, particle-wall mean collision numbers increase by pipe diameter because in larger pipe diameters, the integral time scale of turbulence (τ_L) increase and turbulent dispersion enhanced for smaller particles which result in more collisions with the wall. Similar results were confirmed by (Sommerfeld, 2003).

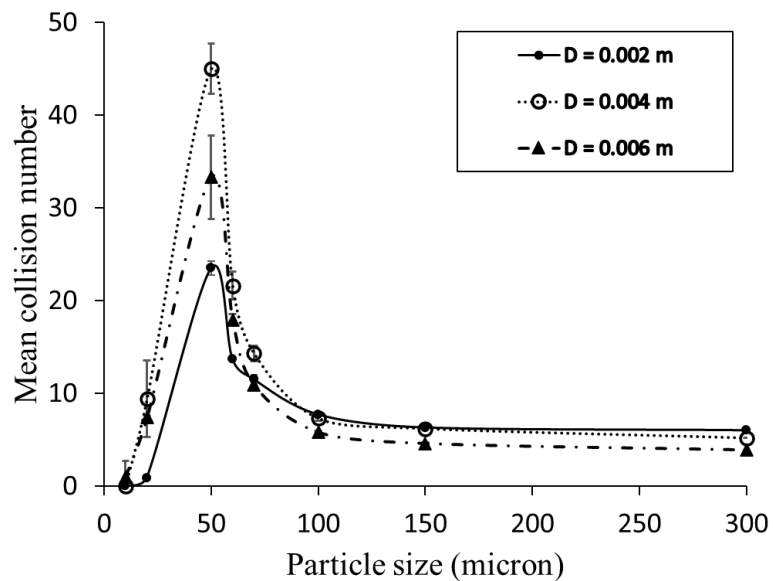


Figure 20. Influence of pipe diameter on particle-wall mean collision number. In all cases particles were released into a 1-meter pipe with 8.4 (m/s) air velocity.

Four different pipe lengths (0.25, 0.5, 1, and 1.5 meters) were used in simulations to investigate the influence of pipe length on the particle-wall mean collision numbers. In all simulations, the pipes' diameter and airflow velocity were 4.76 mm and 8.4 ms⁻¹. For particles with different sizes which released in the pipe with 0.25-meter length, the calculated mean collision numbers are almost similar, i.e., less than one collision per particle, which means that in such condition, almost all particles exit the pipe without colliding with the pipe wall. By increasing the pipe length to 0.5-meter, different particle sizes showed different mean collision numbers, but there is still no significant difference between various particle sizes in terms of the calculated mean collision number. For particles released in a 1-meter length pipe, there is a clear difference in recorded mean collision numbers for different particle sizes. Based on these results, the minimum pipe length for investigating particle size's effect on mean collision numbers is 1-meter pipe length because, in shorter pipes, all particle sizes show almost similar interactions with the wall. By increasing the pipe length to 1.5 meters, the mean collision numbers for particles larger than 100 microns increase as the particle's residence time increases. However, for particles smaller than 100 microns, as particle motion is affected by turbulent structures, the slope of this augmentation is very high (Figure 21).

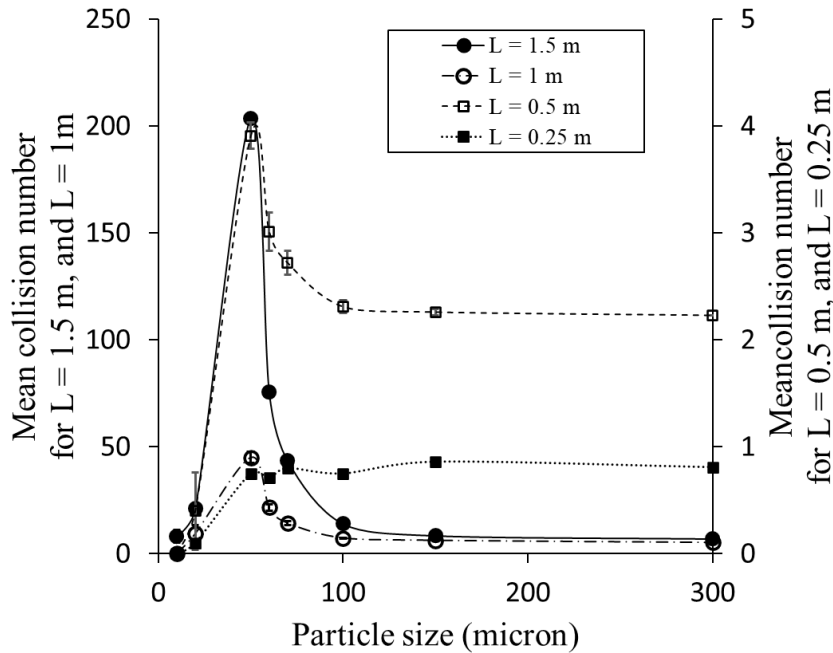


Figure 21. Influence of pipe length on particle-wall interactions. In all cases particles were released into a pipe with 4.76 mm inner diameter and 8.4 (ms^{-1}) air velocity.

4.6. Influence of air velocity on particle-wall interactions

For examining the impact of air velocity on particle-wall interactions, particles of different sizes were released into pipe flows with different air velocities. The calculated mean collision numbers were also compared in a laminar and turbulent flow. The pipe dimension used for simulations was 1 meter in length and 0.00476 meters in diameter in all cases. One hundred particles were released in every simulation, and the average collision number was expressed as the mean collision number.

Simulation results confirmed that particle-wall mean collision number and air velocity are inversely related (Figure 22). Comparing particles with similar size traveling in different air velocities confirmed that more particle-wall interaction occurs in lower air velocity, whereas in higher air velocity, particles barely collide with the pipe wall before exiting the pipe. These results are likely to be related to

particle residence time in the pipe flow. Results also show that particle-wall mean collision numbers decrease by particle size expectedly in lower air velocities. Interestingly, in very high air velocities (36 ms^{-1}), large particles showed more collisions than smaller sizes. The possible reason might be that those smaller particles passing through high air velocities trapped at the center eddies of the pipe flow and exit the pipe before gravity force pulls them towards the pipe wall.

Furthermore, to investigate the effect of turbulence on particle-wall interactions, a laminar flow with 6.5 ms^{-1} air velocity was compared with turbulent flows in higher velocities. Figure 22 shows that the particle-wall mean collision number in laminar flow is higher than the turbulent flows with 15 and 36 ms^{-1} due to higher particle residence time, but it shows fewer interactions than turbulent flow with 8.4 ms^{-1} air velocity.

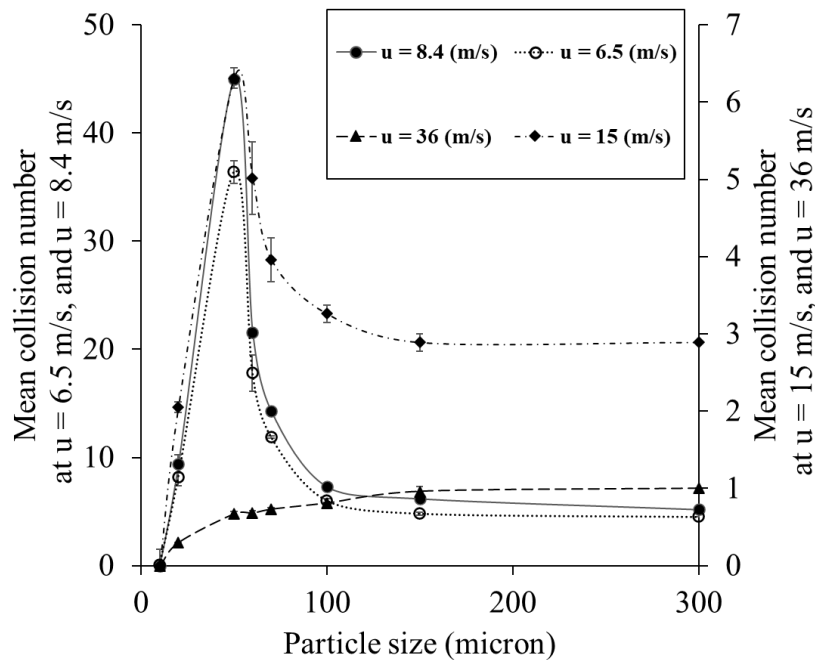


Figure 22. Influence of air velocity on particle-wall mean collision numbers. All calculations were accomplished for a single pipe length (1 m), and diameter (4.76 mm).

4.7. ANN model for predicting particle-wall interactions

4.7.1. Number of neurons in the hidden layer

For deciding the optimal number of neurons in the hidden layer (Layer 2) to avoid the model from underfitting and overfitting, an optimization analysis was performed in MATLAB. In this analysis, the number of neurons in the hidden layer (Layer 2) was altered from 1 to 10. The root mean square error (RMSE) of each network was calculated five times, and the average value was considered as the performance of the generated networks.

Figure 23 demonstrates the RMSEs of different networks as a function of the number of neurons in the hidden layer. It is clear from the graph that using only one neuron in Layer 2 makes the model under-fitted, which means that the model fails to capture the key trends during the training process. It can be concluded from the graph that using 6 neurons in Layer 2 is good enough to confirm a sufficient accuracy of the model performance.

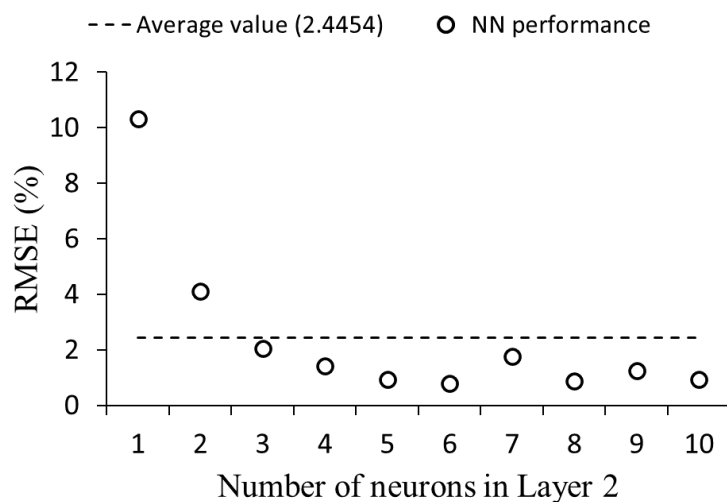


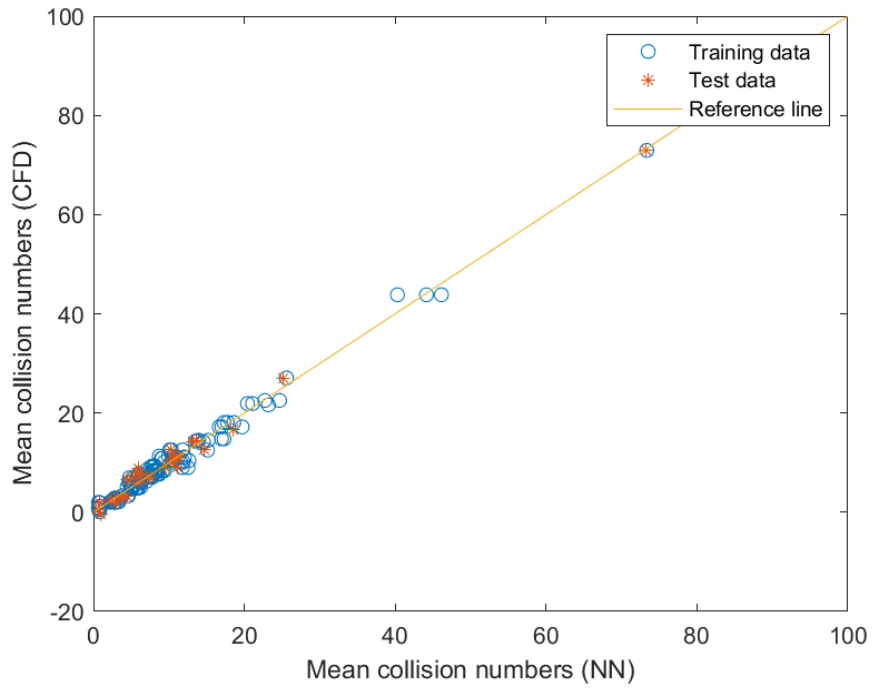
Figure 23. Influence of number neurons in the second layer on network performance.

4.7.2. Network testing and model validation

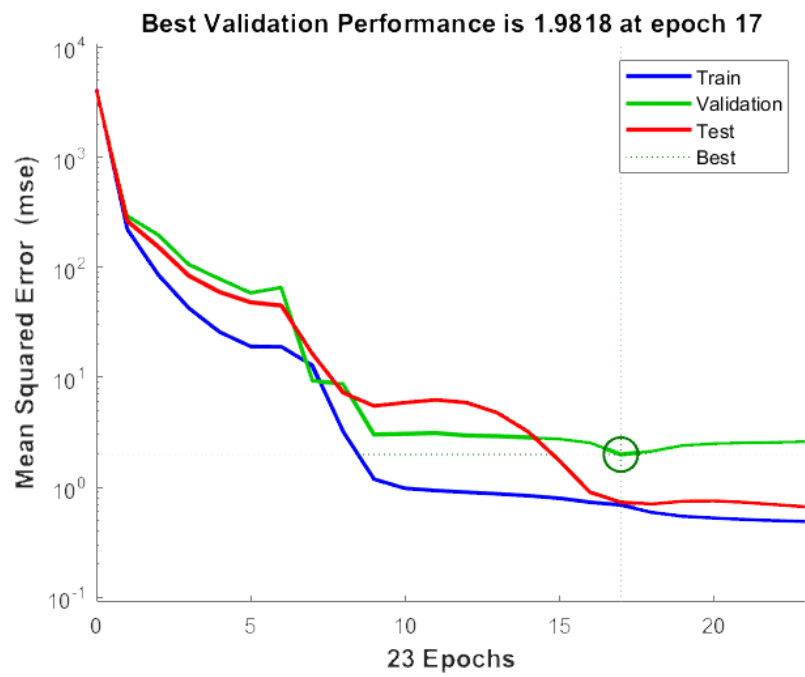
The test set, which contains 15 % of the database, was employed for evaluating the neural network performance. The test set includes new data for the model, and the model has not trained on them in the training process. Figure 24a demonstrates the model's performance for the training set and the test set. The best validation performance of the model is shown in Figure 24b with the mean squared error performance function. The best validation performance is 1.98 at epoch 17.

However, different networks with different performances are created due to different initial weights and bias values used for the training process. Therefore, for evaluating the model performance, 30 neural networks with various initial weights and bias values were generated using the same training data set. The neural network prediction values of the test set were expressed as the average output values of all 30 networks. Figure 25 shows the error of all 30 networks on predicting the test set values. The average value of RMSE for all networks is very low (0.94), which shows the model's high performance in predicting mean collision numbers for the test set.

Figure 26 demonstrates the regression analysis chart for the mean square error (MSE) performance function. The calculated R for the training set is 0.98, the validation error is 0.99, and the testing error is 0.98. Based on this information, it is evident that the proposed model can predict particle-wall mean collision numbers based on particle and flow physical parameters in particle-laden pipe flows with high accuracy.



a)



b)

Figure 24. Comparing mean collision numbers calculated with CFD and predictions of the neural network (a), performance plot of the model (b).

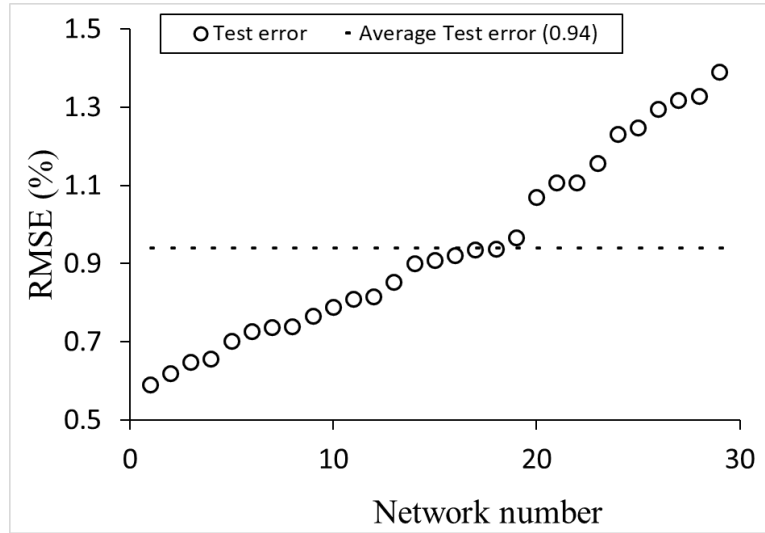


Figure 25. The average performance of the neural network.

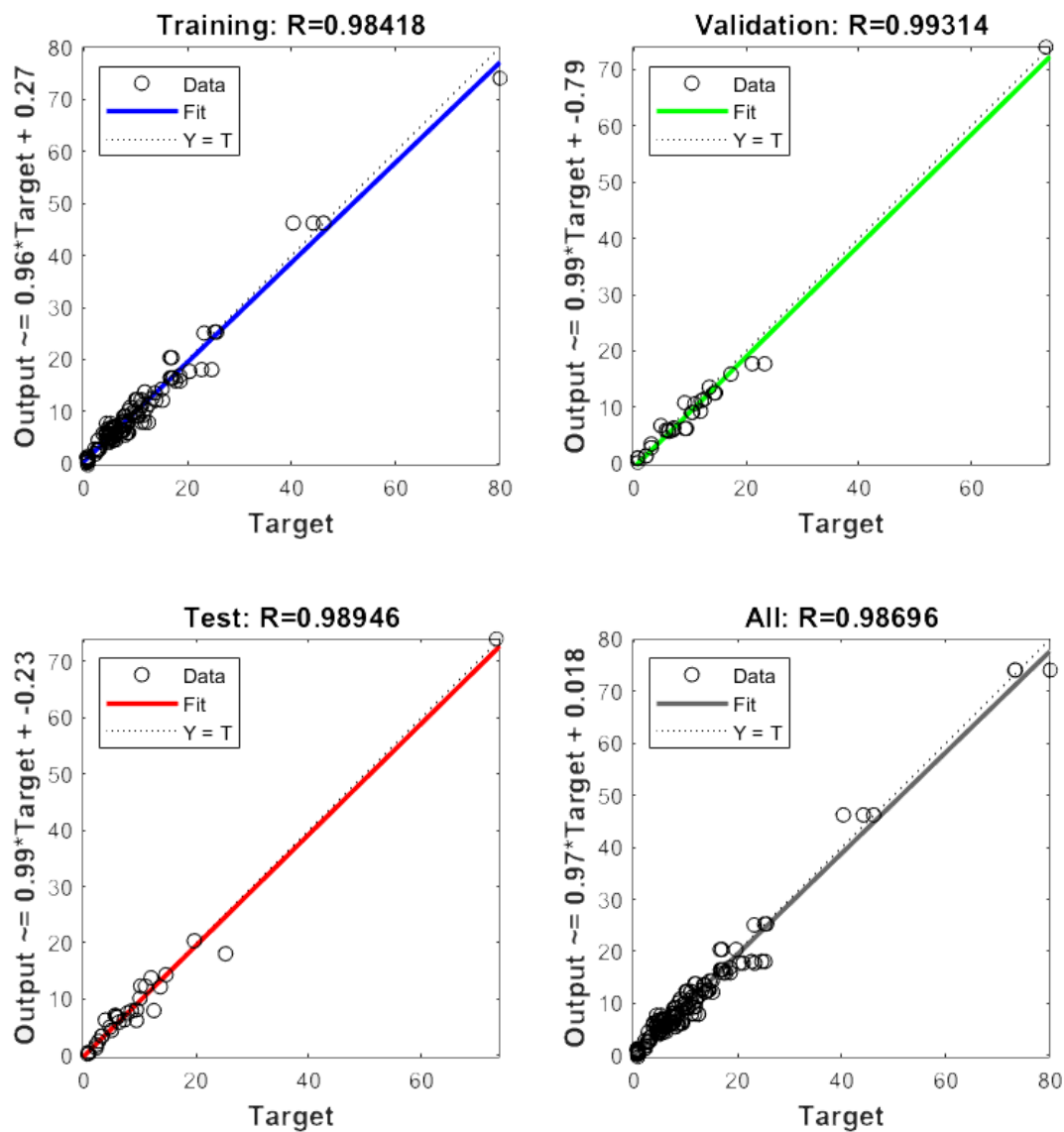


Figure 26. Regression analysis chart.

4.8. Tribocharging model

4.8.1. Experimental charge measurement results

Table 8 shows the charge to mass ratio of particles with different diameters. These data were obtained by the researchers at Howard University using the experimental

procedure described in chapter 3 of this thesis. The lowest charge to mass ratio gained via tribocharging belongs to the small particles with 25-micron (micrometer) diameter, whereas particles with approximately 60-micron (61.7 micron to be exact) diameter show an extremely high charge to mass ratio after tribocharging. At the same time, the measured charge to mass ratio for 60-micron particles show the highest standard deviation during different experimental runs. For particles larger than 60-micron, the amount of charge to mass gained by the particles during tribocharging drops suddenly for 86-micron particles and gradually decreases for particles larger than 200-micron.

Table 8. Experimental charge measurement results for yellow pea powder dispersed into a PTFE tribocharger tube (1.5 m length, and 4.76 mm inner diameter) using air (6.5 ms⁻¹ velocity) as the carrier fluid.

Particle Diameter (micron)	Charge to Mass Ratio (nC/g)	
	AVG	STD
380.9	157.9	27.8
252.7	231.2	74.9
192.7	314.5	71.6
138.9	323.8	69.1
86.3	307.8	78.3
61.7	608.8	151.3
25	138.2	49.5

4.8.2. Influence of particle wall interactions on tribocharging in laminar particle-laden flows

The experimental results of charge measurements were obtained by releasing particles into a laminar pipe flow with 6.5 ms⁻¹ air velocity. Therefore, a numerical simulation was conducted to compute particle-wall interactions in a laminar flow with the exact boundary conditions used in the experiments. Accordingly, 100 particles of identical size were released into a horizontal pipe with 1.5 m length and 4.76 mm inner diameter, and 6.5 ms⁻¹ air velocity. The drag and gravity were the

dominant forces exerted on particles. The number of particle-wall collisions was determined by defining an auxiliary dependent variable on each particle that updated the collision number every time each particle collided with the pipe wall. The average of collisions computed for each particle was reported as the particle-wall mean collision number.

Figure 27 demonstrates the calculated mean collision numbers for different particle sizes. Although no turbulence effect exists in this simulation, this graph presents a similar trend as reported for particles transported in a turbulent flow (Figure 18). Results confirmed that small particles (< 40 microns) have the lowest collision number, whereas medium size particles ($40 \text{ microns} < D_p < 100 \text{ microns}$) show maximum particle-wall interactions as it was also reported for intermediate Stokes particles in a turbulent particle-laden flow. For particles larger than 100 microns, the particle-wall mean collision numbers do not show significant deviation by particle size.

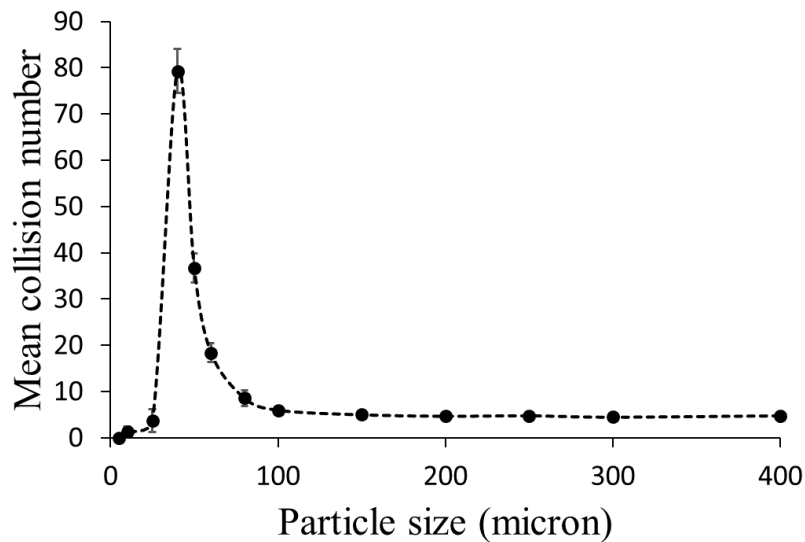
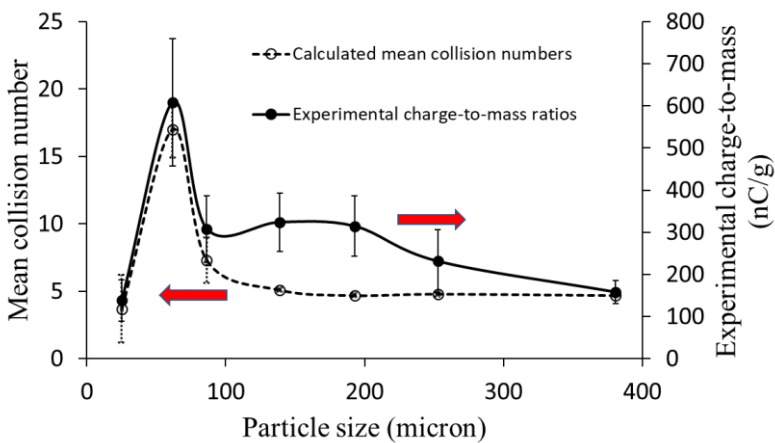
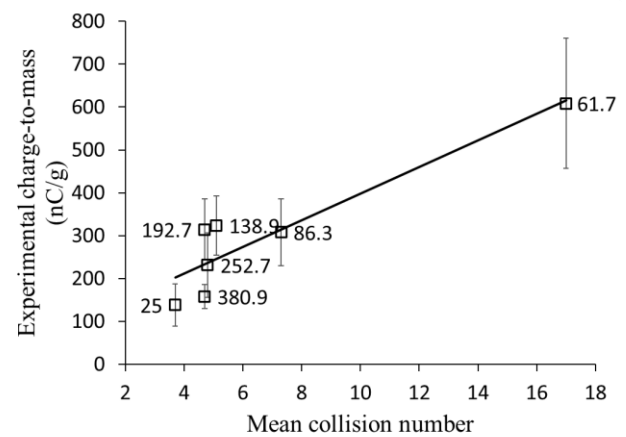


Figure 27. Computed particle-wall mean collision numbers for different particle sizes released into a pipe with 1.5 (m) length and 4.76 (mm) inner diameter and 6.5 (m/s) air velocity (Reynolds = 1900).

Figure 28a describes the influence of particle size on the particle-wall mean collision numbers and the experimentally measured charge to mass ratios. The lowest charge to mass ratio was reported for small particles with a 25-micron diameter having the minimum mean collision number (3.7 collisions per particle) in this graph. Conversely, the maximum amount of charge to mass ratio was reported for 60-micron particles having the highest rate of particle-wall mean collision number (17 collisions per particle). For larger particles, the measured charge to mass ratio decreases exponentially due to fewer particle-wall interactions, and for particles larger than 100 microns, the charge to mass ratios do not change dramatically as the collision numbers are almost identical. The correlation between the experimental charge measurement values and the computed particle-wall mean collision numbers for different particle sizes is illustrated in Figure 28b. These results confirm the correlation between particles charging rate and the number of particle-wall interactions. Hence, particle-wall collision number computed based on different particle and flow properties is a potent parameter for modeling particle tribocharging in particle-laden flows.



a)



b)

Figure 28. a) Effect of particle size on mean collision number and charge to mass ratio, b) the correlation of experimental charge to mass ratios and particle-wall mean collision numbers. Data labels and error bars show the particle size and deviation of charge measurements during multiple experimental runs.

4.8.3. Influence of material on tribocharging

Material of the contact bodies significantly affects the tribocharging process (Itakura *et al.*, 1996; Mazumder *et al.*, 2006; Biegaj *et al.*, 2017). This fact has been applied as a tool for tribo-separation of macroparticles in the recycling industry (Pearse and Hickey, 1978; Dodbiba and Fujita, 2004; Zenkiewicz, Zuk and Markiewicz, 2015; Yang *et al.*, 2019) and tribo-separation of microparticles such as protein and starch particles on a lab-scale (Tabtabaei *et al.*, 2016; Wang *et al.*, 2016; Landauer and Foerst, 2018).

In this study, numerical modeling of particle tribocharging was conducted based on the particle-wall collision numbers calculated via CFD at different operating conditions. Consequently, the contact potential difference (CPD), which is a function of contact surfaces' work functions and depends on the material, was calculated from the experimental charge measurement results using equation 3.21 in chapter 3. Figure 29 demonstrates the correlation of measured charge-to-mass ratios and calculated CPD values for samples with different protein contents. Results also confirm that the value of contact potential difference increases by protein content of the samples. It is clear from the graph that the charge to mass ratio of particles is strongly correlated to the contact potential difference explaining the high charging tendency of powders with higher protein content.

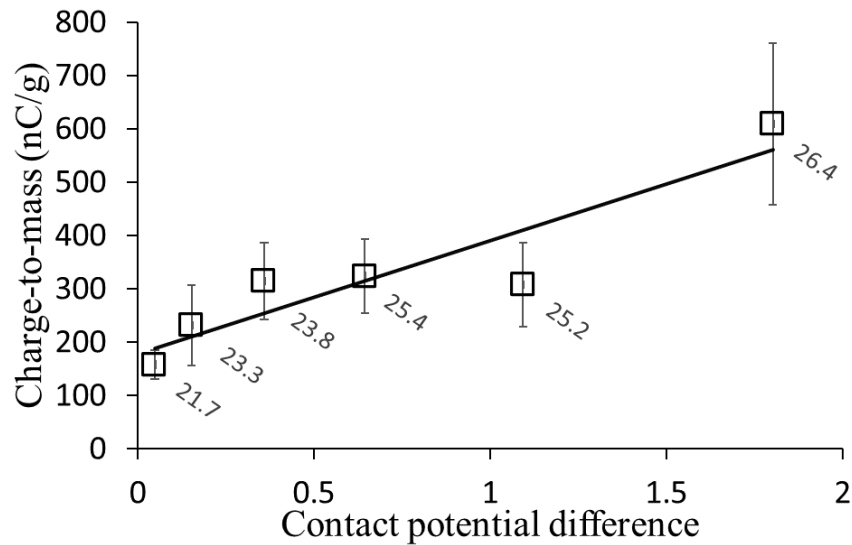


Figure 29. Correlation of experimentally measured charge-to-mass ratios with calculated contact potential difference for samples with different protein content percentages (data labels). Error bars address the deviation of charge measurements during multiple experimental runs.

Based on the calculated values of contact potential difference, the charge-to-mass ratio of particles was calculated for similar particles sizes but at a different air velocity (8.4 ms^{-1}). The number of particle-wall collisions was computed using the CFD model. Figure 30 compares the calculated charge-to-mass ratios at the air velocity of 8.4 ms^{-1} with the experimentally measured values for different particle sizes at 6.5 ms^{-1} . Results show that the calculated charge-to-mass ratios at 8.4 ms^{-1} follow a similar trend to the experimentally measured charge at 6.5 ms^{-1} air velocity but a higher charge value due to higher particle-wall collisions (as was previously shown in Figure 22). Therefore, for a specific combination of particle-wall material, the charge-to-mass of particles passing through a pipe could be estimated based on the particle size and vice versa. Therefore, particle charge measurement during powder transport in particle-laden flows could be used as a novel and yet cost-effective approach for online particle size characterization (see the next section for details). This method could be used as a predictive tool applying particle-laden flows, including pneumatic

conveying of powders in the food and pharmaceutical industries where particle size variation due to agglomeration and segregation during transport is a substantial issue affecting the quality of the final products.

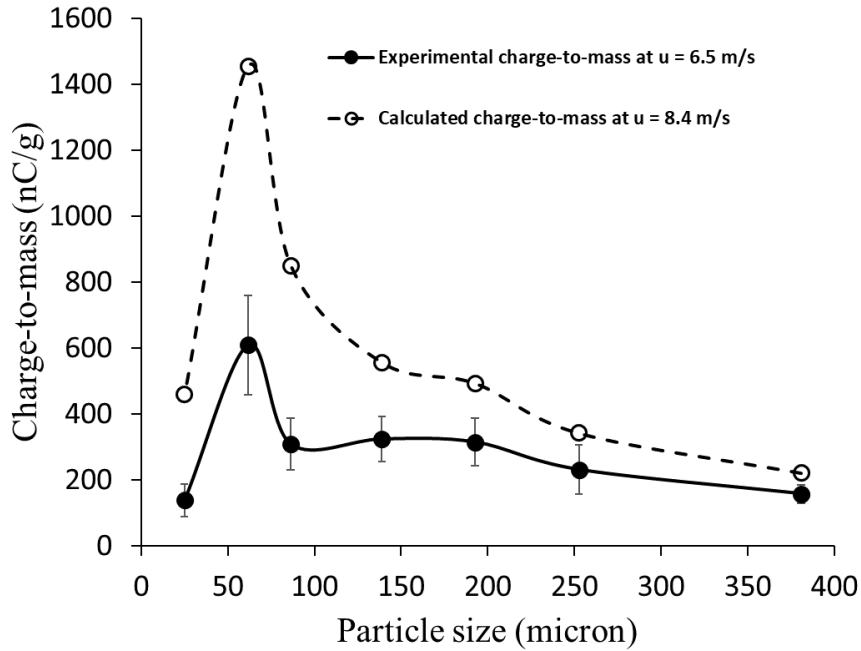


Figure 30. Measured and simulated charge-to-mass ratios for different particle sizes. The pipe material is PTFE ($l = 1.5$ m, $d = 4.76$ mm) and particles are organic flour ($\rho = 1440$ kgm⁻³).

4.8.4. Application of the numerical model

As was discussed previously, the numerical model developed for tribocharging of particles in particle-laden flows is suitable for simulating the charge generation experienced by different particle sizes of similar material. Furthermore, a strong correlation was observed between the values of calculated contact potential difference for samples with different protein contents and the corresponding measured charge-to-mass ratios (Figure 29). Hence, online characterization of powders, such as particle size determination and concentration of various constituents (for example protein content), during transport in particle-laden pipe

flows could be a novel application of the proposed numerical model. Developing a rapid, cost effective, and non-destructive method for online monitoring of powder concentrations is sought after in the pharmaceutical industry, food fraud assessment, and quality control of particulate products. Therefore, investigating the charging behavior of powders during tribocharging in particle-laden flows could be a powerful technique for identifying the chemical composition and concentration of powders' constituents. However, future works are required for understanding the tribocharging behavior of powders with different materials and the influence of different chemical concentrations on powder charging during transport in pipes with different materials.

Figure 31 illustrates a flowchart describing an algorithm created for particle size characterization and powder composition analysis based on the measured charge-to-mass ratios. For a specific particle size, this algorithm could be used for calculation of the contact potential difference which is correlated to the work function and chemical composition of powders. In case of an unknown particle size, this algorithm could be used as a particle size characterization tool for a particular material with specific work function. The algorithm starts with a guessed value for the particle size based on the measured charge-to-mass ratio and feeds it into the CFD-based artificial neural network model for estimating the number of particle-wall collisions. The ANN model search for the best match value of particle-wall collision number based on the model inputs such as air velocity, pipe diameter and length. Consequently, the estimated collision number is used to calculate the charge-to-mass ratio for the guessed particle size. Next, the algorithm compares the calculated and the measured values of the charge-to-mass ratio. The optimal criteria for the model is minimizing the error percentage between the measured and the calculated values of charge to mass ratio. Therefore, if the sum of errors exceeds the predefined threshold, the algorithm guesses a new particle size until it reaches the desired accuracy. More studies and experiments are required to expand the application of this algorithm for industrial cases, such as investigating the influence of different powder materials, pipe geometry

and bends, the surface roughness of pipes, impurities, particle shape, and external electric fields on tribocharging in particle-laden flows.

In the next chapter, chapter five, the overall conclusions of this research and the potential of charge measurements during tribocharging of powders in particle-laden pipe flow for rapid characterization of powders' physical and chemical properties are presented.

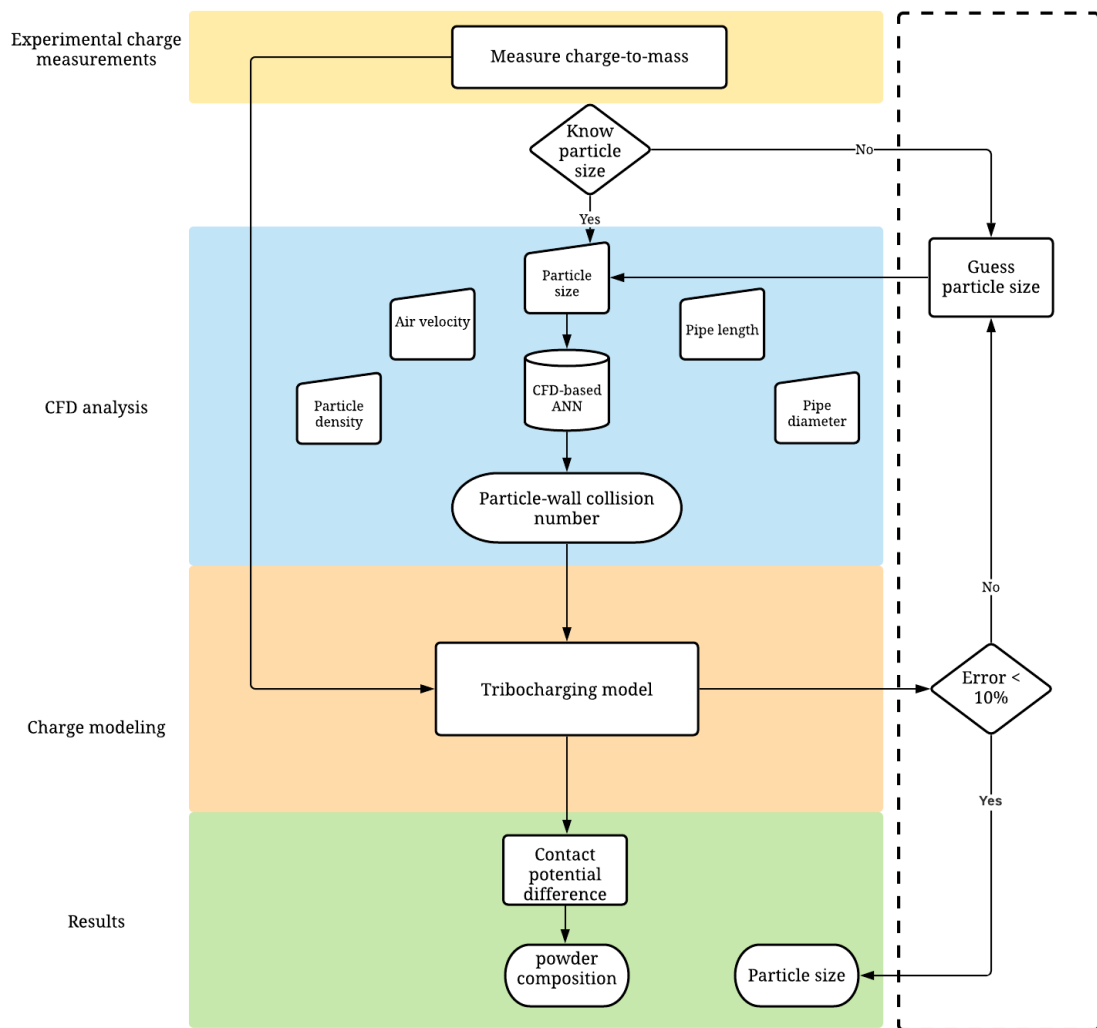


Figure 31. Flowchart describing an algorithm for powder characterization based on particle charge-to-mass.

Chapter 5. Conclusions

The mechanism of powder tribocharging due to repeated particle-wall collision during transport in dilute particle-laden flows was analyzed. Polydisperse powder samples with different protein and starch contents and particle sizes were analyzed to understand the influence of powders' physical and chemical properties as well as the hydrodynamics characteristics of the system on the generated charge after contacting the PTFE pipe wall. Computational fluid dynamics was utilized for numerical simulation of particle trajectories in gas-solid two-phase flows, and the influence of particle size and density, pipe diameter and length, and air velocity on particle-wall mean collision numbers was elucidated. An artificial neural network model was developed for predicting the particle-wall mean collision numbers based on the database generated via CFD simulations. The potential difference between the contact surfaces was calculated according to the experimental charge measurement results and the estimated number of particle-wall collisions.

According to experimental results, there was a nonlinear correlation between the particle size and the measured charge-to-mass ratios. The minimum charge-to-mass ratio was reported for particles with 25 microns in diameter. The maximum charge-to-mass ratio was observed for 60-micron particles, but the charge-to-mass ratio decreased for larger particles. A similar trend was observed for particle-wall mean collision numbers calculated through numerical simulation for different particle diameters, explaining the experimental charge measurement results.

The contact potential difference between the contact surfaces depends on the physicochemical properties of the contact material and requires costly laboratory equipment and a controlled environment to measure. In this study, the contact potential difference was calculated from the experimental charge measurement data and the CFD and tribocharging models. The results from this study also revealed a strong correlation between the calculated contact potential difference and the protein

content of powder samples. Since the charge-to-mass ratio increases directly by the contact potential difference, charge measurement during powder transport in particle-laden flows could be used as a novel approach for the rapid and cost-effective characterization of powders' physical and chemical properties (e.g., particle size or protein content).

To conclude, powder tribocharging during transport in particle-laden flows is strongly affected by the physical and chemical properties of powders. Although powder tribocharging during transport is often considered a nuisance phenomenon such as dust explosion, it could be utilized as an accessible and powerful tool for manipulating powders characteristics if well understood and controlled. It is time to think of this mysterious natural phenomenon not only as a negative issue that should be avoided but as an endless source of energy that could be utilized in various applications.

References

- Di Anibal, C. V., Callao, M. P. and Ruisánchez, I. (2011) '1H NMR and UV-visible data fusion for determining Sudan dyes in culinary spices', *Talanta*. doi: 10.1016/j.talanta.2011.02.014.
- Anochi, J. A. and De Campos Velho, H. F. (2015) 'Optimization of feedforward neural network by Multiple Particle Collision Algorithm', in *IEEE SSCI 2014 - 2014 IEEE Symposium Series on Computational Intelligence - FOCI 2014: 2014 IEEE Symposium on Foundations of Computational Intelligence, Proceedings*. doi: 10.1109/FOCI.2014.7007817.
- Bailey, A. G. (1984) 'Electrostatic phenomena during powder handling', *Powder Technology*. doi: 10.1016/0032-5910(84)80007-8.
- Bailey, A. G. (1998) 'The science and technology of electrostatic powder spraying, transport and coating', *Journal of Electrostatics*. doi: 10.1016/S0304-3886(98)00049-7.
- Baytekin, H. T. *et al.* (2011) 'The mosaic of surface charge in contact electrification', *Science*. doi: 10.1126/science.1201512.
- Biegaj, K. W. *et al.* (2017) 'Surface Chemistry and Humidity in Powder Electrostatics: A Comparative Study between Tribocharging and Corona Discharge', *ACS Omega*. doi: 10.1021/acsomega.7b00125.
- Bocksell, T. L. and Loth, E. (2006) 'Stochastic modeling of particle diffusion in a turbulent boundary layer', *International Journal of Multiphase Flow*. doi: 10.1016/j.ijmultiphaseflow.2006.05.013.
- Cangialosi, F. *et al.* (2006) 'Monte Carlo simulation of pneumatic tribocharging in two-phase flow for high-inertia particles', *Powder Technology*. doi: 10.1016/j.powtec.2006.03.009.

Capecelatro, J. and Desjardins, O. (2013) 'An Euler-Lagrange strategy for simulating particle-laden flows', *Journal of Computational Physics*. doi: 10.1016/j.jcp.2012.12.015.

Chan, L. *et al.* (2020) 'Transport of particles in a turbulent rough-wall pipe flow', *Journal of Fluid Mechanics*. doi: 10.1017/jfm.2020.821.

Chang, Y. P., Chu, H. M. and Chou, H. M. (2007) 'Effects of mechanical properties on the tribo-electrification mechanisms of iron rubbing with carbon steels', *Wear*. doi: 10.1016/j.wear.2006.04.007.

Chen, Y. S. and Kim, S. W. (1987) 'Computation of turbulent flows using an extended k-epsilon turbulence closure model', *NASA STI/Recon Technical Report N*.

Chiesa, M. *et al.* (2005) 'Numerical simulation of particulate flow by the Eulerian-Lagrangian and the Eulerian-Eulerian approach with application to a fluidized bed', *Computers and Chemical Engineering*. doi: 10.1016/j.compchemeng.2004.09.002.

Clarkson, T. G. (1996) 'Introduction to neural networks', *Neural Network World*. doi: 10.1201/9781482277180-13.

Coehn, A. (1898) 'Ueber ein Gesetz der Electricitätserregung', *Annalen der Physik*. doi: 10.1002/andp.18983000203.

Crowe, C. T. *et al.* (2011) *Multiphase Flows with Droplets and Particles*, *Multiphase Flows with Droplets and Particles*. doi: 10.1201/b11103.

Curtis, J. S. and Van Wachem, B. (2004) 'Modeling particle-laden flows: A research outlook', *AIChE Journal*. doi: 10.1002/aic.10394.

Dehbi, A. (2008) 'Turbulent particle dispersion in arbitrary wall-bounded geometries: A coupled CFD-Langevin-equation based approach', *International Journal of Multiphase Flow*. doi: 10.1016/j.ijmultiphaseflow.2008.03.001.

Desjardins, O., Fox, R. O. and Villedieu, P. (2008) 'A quadrature-based moment

- method for dilute fluid-particle flows', *Journal of Computational Physics*. doi: 10.1016/j.jcp.2007.10.026.
- Diaz, A. F. (1998) 'Contact Electrification of Materials: The Chemistry of Ions on Polymer Surfaces', *Journal of Adhesion*. doi: 10.1080/00218469808011102.
- Diaz, A. F. and Felix-Navarro, R. M. (2004) 'A semi-quantitative tribo-electric series for polymeric materials: The influence of chemical structure and properties', *Journal of Electrostatics*. doi: 10.1016/j.elstat.2004.05.005.
- Diaz, A. F. and Fenzel-Alexander, D. (1993) 'An Ion Transfer Model for Contact Charging', *Langmuir*. doi: 10.1021/la00028a021.
- Dizdar, T. O. *et al.* (2018) 'A new method to produce high voltage static electric load for electrostatic separation – Triboelectric charging', *Powder Technology*. doi: 10.1016/j.powtec.2017.12.065.
- Dodbiba, G. and Fujita, T. (2004) 'Progress in separating plastic materials for recycling', *Physical Separation in Science and Engineering*. doi: 10.1080/14786470412331326350.
- Dreeben, T. D. and Pope, S. B. (1997) 'Probability density function and Reynolds-stress modeling of near-wall turbulent flows', *Physics of Fluids*. doi: 10.1063/1.869157.
- Duraisamy, K., Iaccarino, G. and Xiao, H. (2019) 'Turbulence modeling in the age of data', *Annual Review of Fluid Mechanics*. doi: 10.1146/annurev-fluid-010518-040547.
- Dwari, R. K. and Rao, K. H. (2007) 'Dry beneficiation of coal - A review', *Mineral Processing and Extractive Metallurgy Review*. doi: 10.1080/08827500601141271.
- Elghobashi, S. (1991) 'Particle-laden turbulent flows: direct simulation and closure models', *Applied Scientific Research*. doi: 10.1007/BF02008202.

- Elghobashi, S. (1994) 'On predicting particle-laden turbulent flows', *Applied Scientific Research*. doi: 10.1007/BF00936835.
- Ema, A. *et al.* (2003) 'Tribo-charge and rebound characteristics of particles impact on inclined or rotating metal target', *Powder Technology*. doi: 10.1016/S0032-5910(03)00153-0.
- Ferrante, A. and Elghobashi, S. (2003) 'On the physical mechanisms of two-way coupling in particle-laden isotropic turbulence', *Physics of Fluids*. doi: 10.1063/1.1532731.
- Friedrich, R. *et al.* (2001) 'Direct numerical simulation of incompressible turbulent flows', *Computers and Fluids*. doi: 10.1016/S0045-7930(01)00006-8.
- Gallo, C. F., Lama, W. L. and Lama, W. L. (1976) 'Classical Electrostatic Description of the Work Function and Ionization Energy of Insulators', *IEEE Transactions on Industry Applications*. doi: 10.1109/TIA.1976.349379.
- Gamahara, M. and Hattori, Y. (2017) 'Searching for turbulence models by artificial neural network', *Physical Review Fluids*. doi: 10.1103/PhysRevFluids.2.054604.
- Ghanou, Y. and Bencheikh, G. (2016) 'Architecture optimization and training for the multilayer perceptron using ant system', *IAENG International Journal of Computer Science*.
- Gheziel, A., Hanini, S. and Mohamedi, B. (2021) 'Artificial neural network (ANN) for prediction indoor airborne particle concentration', *International Journal of Ventilation*. doi: 10.1080/14733315.2021.1876408.
- Gibson, N. (1997) 'Static electricity - An industrial hazard under control?', *Journal of Electrostatics*. doi: 10.1016/S0304-3886(97)00010-7.
- Gidaspow, D. (2012) *Multiphase Flow and Fluidization: Continuum and Kinetic Theory Descriptions, Multiphase Flow and Fluidization: Continuum and Kinetic Theory*

Descriptions. doi: 10.1016/C2009-0-21244-X.

Glor, M. (2003) 'Ignition hazard due to static electricity in particulate processes', *Powder Technology*. doi: 10.1016/j.powtec.2003.08.017.

Grosshans, H. and Papalexandris, M. V. (2017) 'Direct numerical simulation of triboelectric charging in particle-laden turbulent channel flows', *Journal of Fluid Mechanics*. doi: 10.1017/jfm.2017.157.

Grossi, M. D., Kubat, M. and Özgökmen, T. M. (2020) 'Predicting particle trajectories in oceanic flows using artificial neural networks', *Ocean Modelling*. doi: 10.1016/j.ocemod.2020.101707.

Hao, T. *et al.* (2013) 'Probing pharmaceutical powder blending uniformity with electrostatic charge measurements', *Powder Technology*. doi: 10.1016/j.powtec.2013.04.032.

Henniker, J. (1962) 'Triboelectricity in polymers', *Nature*. doi: 10.1038/196474a0.

Hersh, S. P., Sharman, E. P. and Montgomery, D. J. (1954) 'Static Electrification of Filaments', *Textile Research Journal*. doi: 10.1177/004051755402400506.

Huber, N. and Sommerfeld, M. (1998) 'Modelling and numerical calculation of dilute-phase pneumatic conveying in pipe systems', *Powder Technology*. doi: 10.1016/S0032-5910(98)00065-5.

Iliopoulos, I., Mito, Y. and Hanratty, T. J. (2003) 'A stochastic model for solid particle dispersion in a nonhomogeneous turbulent field', *International Journal of Multiphase Flow*. doi: 10.1016/S0301-9322(02)00165-9.

Ireland, P. M. (2010) 'Triboelectrification of particulate flows on surfaces: Part I - Experiments', *Powder Technology*. doi: 10.1016/j.powtec.2009.11.017.

Itakura, T. *et al.* (1996) 'The contact potential difference of powder and the tribo-charge', *Journal of Electrostatics*. doi: 10.1016/S0304-3886(96)00026-5.

- Jing, Q. *et al.* (2014) 'Case-encapsulated triboelectric nanogenerator for harvesting energy from reciprocating sliding motion', *ACS Nano*. doi: 10.1021/nn500694y.
- Johnson, K. L. (1989) 'Contact Mechanics'. doi: 10.1201/b17588-12.
- Kalitzin, G. *et al.* (2005) 'Near-wall behavior of RANS turbulence models and implications for wall functions', *Journal of Computational Physics*. doi: 10.1016/j.jcp.2004.10.018.
- Kallio, G. A. and Reeks, M. W. (1989) 'A numerical simulation of particle deposition in turbulent boundary layers', *International Journal of Multiphase Flow*. doi: 10.1016/0301-9322(89)90012-8.
- Kamra, A. K. (1972) 'Physical sciences: Visual observation of electric sparks on gypsum dunes', *Nature*. doi: 10.1038/240143a0.
- Karner, S. and Urbanetz, N. A. (2012) 'Arising of electrostatic charge in the mixing process and its influencing factors', *Powder Technology*. doi: 10.1016/j.powtec.2012.04.062.
- Kartushinsky, A. *et al.* (2016) 'Eulerian-Eulerian modelling of particle-laden two-phase flow', *Powder Technology*. doi: 10.1016/j.powtec.2016.07.053.
- Korevaar, M. W. *et al.* (2014) 'Integrated DEM-CFD modeling of the contact charging of pneumatically conveyed powders', *Powder Technology*. doi: 10.1016/j.powtec.2014.03.020.
- Lacks, D. J. and Mohan Sankaran, R. (2011) 'Contact electrification of insulating materials', *Journal of Physics D: Applied Physics*. doi: 10.1088/0022-3727/44/45/453001.
- Lain, S., Sommerfeld, M. and Kussin, J. (2002) 'Experimental studies and modelling of four-way coupling in particle-laden horizontal channel flow', *International Journal of Heat and Fluid Flow*. doi: 10.1016/S0142-727X(02)00160-1.

- Landauer, J. and Foerst, P. (2018) 'Triboelectric separation of a starch-protein mixture – Impact of electric field strength and flow rate', *Advanced Powder Technology*. doi: 10.1016/j.appt.2017.10.018.
- Langevin, P. (1908) 'Sur la theorie du mouvement brownien', *C.R. Acad. Sci., (Paris)*.
- Laurentie, J. C., Traoré, P. and Dascalescu, L. (2013) 'Discrete element modeling of triboelectric charging of insulating materials in vibrated granular beds', *Journal of Electrostatics*. doi: 10.1016/j.elstat.2013.08.001.
- Lew, A. J., Buscaglia, G. C. and Carrica, P. M. (2001) 'A Note on the Numerical Treatment of the k-epsilon Turbulence Model', *International Journal of Computational Fluid Dynamics*. doi: 10.1080/10618560108940724.
- Luo, Z. *et al.* (2003) 'Progress in dry coal cleaning using air-dense medium fluidized beds', in *International Journal of Coal Preparation and Utilization*. doi: 10.1080/07349340302267.
- Marchioli, C. and Soldati, A. (2002) 'Mechanisms for particle transfer and segregation in a turbulent boundary layer', *Journal of Fluid Mechanics*. doi: 10.1017/S0022112002001738.
- Masuda, H. *et al.* (1995) 'The measurement and evaluation of the contact potential difference between various powders and a metal', *Advanced Powder Technology*. doi: 10.1016/S0921-8831(08)60519-1.
- Masuda, H. *et al.* (1998) 'Electrification of fine particles in gas-solids pipe flow', *KONA Powder and Particle Journal*. doi: 10.14356/kona.1998024.
- Masuda, H., Komatsu, T. and Iinoya, K. (1976) 'The static electrification of particles in gas-solids pipe flow', *AIChE Journal*. doi: 10.1002/aic.690220320.
- Matsusaka, S. *et al.* (2002) 'Electrostatic charge distribution of particles in gas-solids pipe flow', *Journal of Electrostatics*. doi: 10.1016/S0304-3886(01)00185-1.

Matsusaka, S. *et al.* (2008) 'Analysis of pulsating electric signals generated in gas-solids pipe flow', *Chemical Engineering Science*. doi: 10.1016/j.ces.2007.07.010.

Matsusaka, S *et al.* (2010) 'Triboelectric charging of powders : A review', *Chemical Engineering Science*. Elsevier, 65(22), pp. 5781–5807. doi: 10.1016/j.ces.2010.07.005.

Matsusaka, S. *et al.* (2010) 'Triboelectric charging of powders: A review', *Chemical Engineering Science*. doi: 10.1016/j.ces.2010.07.005.

Matsusaka, S., Ghadiri, M. and Masuda, H. (2000) 'Electrification of an elastic sphere by repeated impacts on a metal plate', *Journal of Physics D: Applied Physics*. doi: 10.1088/0022-3727/33/18/316.

Matsusaka, S. and Masuda, H. (2003) 'Electrostatics of particles', *Advanced Powder Technology*. doi: 10.1163/156855203763593958.

Matsusaka, S. and Masuda, H. (2006) 'Simultaneous measurement of mass flow rate and charge-to-mass ratio of particles in gas-solids pipe flow', in *Chemical Engineering Science*. doi: 10.1016/j.ces.2005.05.006.

Matsuyama, T. *et al.* (2003) 'Impact charging experiments with single particles of hundred micrometre size', *Powder Technology*. doi: 10.1016/S0032-5910(03)00154-2.

Matsuyama, T. and Yamamoto, H. (1995) 'Charge relaxation process dominates contact charging of a particle in atmospheric conditions', *Journal of Physics D: Applied Physics*. doi: 10.1088/0022-3727/28/12/005.

Matsuyama, T. and Yamamoto, H. (1997) 'Charge-relaxation process dominates contact charging of a particle in atmospheric condition: II. the general model', *Journal of Physics D: Applied Physics*. doi: 10.1088/0022-3727/30/15/008.

Mazumder, M. K. *et al.* (2006) 'Twenty-first century research needs in electrostatic

processes applied to industry and medicine', in *Chemical Engineering Science*. doi: 10.1016/j.ces.2005.05.002.

McCarty, L. S., Winkleman, A. and Whitesides, G. M. (2007) 'Ionic electrets: Electrostatic charging of surfaces by transferring mobile ions upon contact', *Journal of the American Chemical Society*. doi: 10.1021/ja067301e.

Mi, Y., Ishii, M. and Tsoukalas, L. H. (2001) 'Flow regime identification methodology with neural networks and two-phase flow models', *Nuclear Engineering and Design*. doi: 10.1016/S0029-5493(00)00325-3.

Miura, T., Koyaguchi, T. and Tanaka, Y. (2002) 'Measurements of electric charge distribution in volcanic plumes at Sakurajima volcano, Japan', *Bulletin of Volcanology*. doi: 10.1007/s00445-001-0182-1.

Moin, P. (1997) 'Progress in large eddy simulation of turbulent flows', in *35th Aerospace Sciences Meeting and Exhibit*. doi: 10.2514/6.1997-749.

Molenda, M. *et al.* (2006) 'Testing mechanical properties of food powders in two laboratories - Degree of consistency of results', *International Agrophysics*.

Multiphase Flow Handbook (2016) *Multiphase Flow Handbook*. doi: 10.1201/9781315371924.

Nifuku, M. and Katoh, H. (2003) 'A study on the static electrification of powders during pneumatic transportation and the ignition of dust cloud', *Powder Technology*. doi: 10.1016/S0032-5910(03)00163-3.

Obukhov, A. M. (1959) 'Description of Turbulence in Terms of Lagrangian Variables', *Advances in Geophysics*. doi: 10.1016/S0065-2687(08)60098-9.

Ohsawa, A. (2003) 'Computer simulation for assessment of electrostatic hazards in filling operations with powder', *Powder Technology*. doi: 10.1016/S0032-5910(03)00162-1.

- Ohsawa, A. (2011) 'Statistical analysis of fires and explosions attributed to static electricity over the last 50 years in Japanese industry', in *Journal of Physics: Conference Series*. doi: 10.1088/1742-6596/301/1/012033.
- Otawara, K. *et al.* (2002) 'An artificial neural network as a model for chaotic behavior of a three-phase fluidized bed', *Chaos, Solitons and Fractals*. doi: 10.1016/S0960-0779(00)00250-2.
- Pai, D. M. and Springett, B. E. (1993) 'Physics of electrophotography', *Reviews of Modern Physics*. doi: 10.1103/RevModPhys.65.163.
- Pai, M. G. and Subramaniam, S. (2009) 'A comprehensive probability density function formalism for multiphase flows', *Journal of Fluid Mechanics*. doi: 10.1017/S002211200900617X.
- Pandya, D. A., Dennis, B. H. and Russell, R. D. (2017) 'A computational fluid dynamics based artificial neural network model to predict solid particle erosion', *Wear*. doi: 10.1016/j.wear.2017.02.028.
- Paschen, F. (1889) 'Ueber die zum Funkenübergang in Luft, Wasserstoff und Kohlensäure bei verschiedenen Drucken erforderliche Potentialdifferenz', *Annalen der Physik*. doi: 10.1002/andp.18892730505.
- Patankar, N. A. and Joseph, D. D. (2001) 'Modeling and numerical simulation of particulate flows by the Eulerian-Lagrangian approach', *International Journal of Multiphase Flow*. doi: 10.1016/S0301-9322(01)00021-0.
- Patel, V. C., Rodi, W. and Scheuerer, G. (1985) 'Turbulence models for near-wall and low reynolds number flows — a review', *AIAA Journal*. doi: 10.2514/3.9086.
- Pearse, M. J. and Hickey, T. J. (1978) 'The separation of mixed plastics using a dry, triboelectric technique', *Resource Recovery and Conservation*. doi: 10.1016/0304-3967(78)90004-5.

- Ramchoun, H. *et al.* (2016) 'Multilayer Perceptron: Architecture Optimization and Training', *International Journal of Interactive Multimedia and Artificial Intelligence*. doi: 10.9781/ijimai.2016.415.
- Robins, E. S., Lowell, J. and Rose-Innes, A. C. (1980) 'The role of surface ions in the contact electrification of insulators', *Journal of Electrostatics*. doi: 10.1016/0304-3886(80)90002-9.
- Rowley, G. (2001) 'Quantifying electrostatic interactions in pharmaceutical solid systems', *International Journal of Pharmaceutics*. doi: 10.1016/S0378-5173(01)00784-0.
- Schein, L. B. (1999) 'Recent advances in our understanding of toner charging', *Journal of Electrostatics*. doi: 10.1016/S0304-3886(98)00056-4.
- Schiller, L. and Naumann, Z. (1935) *A drag coefficient correlation*, *Z.Ver.Deutsch.Ing.* doi: 10.1016/j.ijheatmasstransfer.2009.02.006.
- Schwindt, N. *et al.* (2017) 'Measurement of electrostatic charging during pneumatic conveying of powders', *Journal of Loss Prevention in the Process Industries*. doi: 10.1016/j.jlp.2017.05.028.
- Shinbrot, T., Lamarche, K. and Glasser, B. J. (2006) 'Triboelectrification and razorbacks: Geophysical patterns produced in dry grains', *Physical Review Letters*. doi: 10.1103/PhysRevLett.96.178002.
- Shirakawa, Y. *et al.* (2010) 'Quantum chemical calculation of electron transfer at metal/polymer interfaces', *Advanced Powder Technology*. doi: 10.1016/j.appt.2010.05.007.
- Sommerfeld, M. (2003) 'Analysis of collision effects for turbulent gas-particle flow in a horizontal channel: Part I. Particle transport', *International Journal of Multiphase Flow*. doi: 10.1016/S0301-9322(03)00031-4.

- Sommerfeld, M. and Huber, N. (1999) 'Experimental analysis of modelling of particle-wall collisions', *International Journal of Multiphase Flow*. doi: 10.1016/S0301-9322(99)00047-6.
- Srinivasan, S. and Saghir, M. Z. (2013) 'Modeling of thermotransport phenomenon in metal alloys using artificial neural networks', *Applied Mathematical Modelling*. doi: 10.1016/j.apm.2012.06.018.
- Srinivasan, S. and Saghir, M. Z. (2014a) 'A neurocomputing model to calculate the thermo-solutal diffusion in liquid hydrocarbon mixtures', *Neural Computing and Applications*. doi: 10.1007/s00521-012-1217-6.
- Srinivasan, S. and Saghir, M. Z. (2014b) 'Predicting thermodiffusion in an arbitrary binary liquid hydrocarbon mixtures using artificial neural networks', *Neural Computing and Applications*. doi: 10.1007/s00521-014-1603-3.
- Strömberg, T. *et al.* (2011) 'A modelling study of evolving particle-laden turbulent pipe-flow', in *Flow, Turbulence and Combustion*. doi: 10.1007/s10494-011-9335-2.
- Subramaniam, S. (2013) 'Lagrangian-Eulerian methods for multiphase flows', *Progress in Energy and Combustion Science*. doi: 10.1016/j.pecs.2012.10.003.
- Tabatabaei, S. *et al.* (2016) 'Solvent-free production of protein-enriched fractions from navy bean flour using a triboelectrification-based approach', *Journal of Food Engineering*. doi: 10.1016/j.jfoodeng.2015.11.010.
- Tabatabaei, S. *et al.* (2019) 'Functional properties of navy bean (*Phaseolus vulgaris*) protein concentrates obtained by pneumatic tribo-electrostatic separation', *Food Chemistry*. doi: 10.1016/j.foodchem.2019.01.031.
- Tanoue, K. I. *et al.* (2001) 'Numerical simulation of tribo-electrification of particles in a gas-solids two-phase flow', *Powder Technology*. doi: 10.1016/S0032-5910(01)00302-3.

- Thornton, C. (1997) 'Coefficient of restitution for collinear collisions of elastic-perfectly plastic spheres', *Journal of Applied Mechanics, Transactions ASME*. doi: 10.1115/1.2787319.
- Tsuji, Y. *et al.* (1987) 'Numerical simulation of gas-solid two-phase flow in a two-dimensional horizontal channel', *International Journal of Multiphase Flow*. doi: 10.1016/0301-9322(87)90044-9.
- Uijtewaal, W. S. J. and Oliemans, R. V. A. (1996) 'Particle dispersion and deposition in direct numerical and large eddy simulations of vertical pipe flows', *Physics of Fluids*. doi: 10.1063/1.869046.
- Wang, J. *et al.* (2016) 'Lupine protein enrichment by milling and electrostatic separation', *Innovative Food Science and Emerging Technologies*. doi: 10.1016/j.ifset.2015.12.020.
- Watanabe, H. *et al.* (2007) 'Triboelectrification of pharmaceutical powders by particle impact', *International Journal of Pharmaceutics*. doi: 10.1016/j.ijpharm.2006.11.005.
- Watano, S., Saito, S. and Suzuki, T. (2003) 'Numerical simulation of electrostatic charge in powder pneumatic conveying process', *Powder Technology*. doi: 10.1016/S0032-5910(03)00159-1.
- Wilcox, D. C. (1993) *Turbulence modeling for CFD, Aiaa*.
- Wong, J., Kwok, P. C. L. and Chan, H. K. (2015) 'Electrostatics in pharmaceutical solids', *Chemical Engineering Science*. doi: 10.1016/j.ces.2014.05.037.
- Xiao, H. and Cinnella, P. (2019) 'Quantification of model uncertainty in RANS simulations: A review', *Progress in Aerospace Sciences*. doi: 10.1016/j.paerosci.2018.10.001.
- Yamamoto, H. and Scarlett, B. (1986) 'Triboelectric Charging of Polymer Particles by

Impact', *Particle & Particle Systems Characterization*. doi:
10.1002/ppsc.19860030305.

Yamamoto, Y. *et al.* (2001) 'Large-eddy simulation of turbulent gas-particle flow in a vertical channel: Effect of considering inter-particle collisions', *Journal of Fluid Mechanics*. doi: 10.1017/S0022112001005092.

Yan, Y., Xu, L. and Lee, P. (2006) 'Mass flow measurement of fine particles in a pneumatic suspension using electrostatic sensing and neural network techniques', *IEEE Transactions on Instrumentation and Measurement*. doi:
10.1109/TIM.2006.887040.

Yang, J. *et al.* (2019) 'Recycling organics from non-metallic fraction of waste printed circuit boards by a novel conical surface triboelectric separator', *Resources, Conservation and Recycling*. doi: 10.1016/j.resconrec.2019.03.008.

Young, J. and Leeming, A. (1997) 'A theory of particle deposition in turbulent pipe flow', *Journal of Fluid Mechanics*. doi: 10.1017/S0022112097005284.

Yu, J. *et al.* (2010) 'Kinetics and mechanism of solid reactions in a micro fluidized bed reactor', *AIChE Journal*. doi: 10.1002/aic.12205.

Yuhong, Z. and Wenxin, H. (2009) 'Application of artificial neural network to predict the friction factor of open channel flow', *Communications in Nonlinear Science and Numerical Simulation*. doi: 10.1016/j.cnsns.2008.06.020.

Zenkiewicz, M., Zuk, T. and Markiewicz, E. (2015) 'Triboelectric series and electrostatic separation of some biopolymers', *Polymer Testing*. doi:
10.1016/j.polymertesting.2015.01.009.

Zou, H. *et al.* (2019) 'Quantifying the triboelectric series', *Nature Communications*. doi: 10.1038/s41467-019-09461-x.